



Hot Corrosion Resistance of CeO₂-Doped Cr₃C₂-NiCr Coatings on Austenite Steel Against Molten Salt (Na₂SO₄-60%V₂O₅) Environment

Harkulvinder Singh¹ · Sukhpal Singh Chatha¹ · Buta Singh Sidhu²

Received: 7 June 2022 / Revised: 13 October 2022 / Accepted: 19 October 2022 / Published online: 1 November 2022
© The Author(s), under exclusive licence to Springer Nature Switzerland AG 2022

Abstract

Three ratios of Ce (0.4 wt.%, 0.8 wt.%, and 1.2 wt.%) were added in Cr₃C₂-NiCr powder and coated on TP347H steel with HIPOJET-gun for examining the hot corrosion behaviour in Na₂SO₄-60V₂O₅ salt at 750 °C. The techniques XRD, SEM/EDS, and X-ray mapping were used to analyse the corrosion products. The current work investigates the coating and oxide scale properties in relation to variable RE content. Moreover, the amount of Cr to develop Cr₂O₃ is analysed after the addition of CeO₂ in the coating. Among the three ratios, 0.4 wt.% of CeO₂ in Cr₃C₂-NiCr provided excellent hot corrosion resistance due to the development of a thin oxide scale composed of Cr₂O₃, NiCr₂O₄, Ce₂O₃, and CeCrO₃. From the analysis of corrosion kinetics and microstructure, it has been proposed that the segregation of rare earth (RE) element retards the diffusion of cation (Cr) through Ce₂O₃ and CeCrO₃. However, the hot corrosion protection decreased after the addition of 1.2 wt.% of CeO₂ in the Cr₃C₂-NiCr coating due to increased porosity and inclusions in the oxide scale. The RE-modified HS1, HS3, and HS5 coatings were able to reduce the corrosion rate by 80.34%, 52.05%, and 27.21%, respectively, in comparison with uncoated steel.

Keywords TP347H · Hot corrosion · HVOF · Cr₃C₂-NiCr · Ceria

1 Introduction

High-temperature corrosion (HTC) phenomena play a significant role in the selection of base materials for aerospace, petrochemical, power plants, nuclear reactors, heating furnace, gas turbines, waste incinerators, heat exchangers, extrusion machines, metallurgical plants, etc. [1, 2]. The component's physical, mechanical, and chemical stability is the first requirement for every industry and organization. HTC study is a common subject; therefore, it is of great importance to increase our knowledge about the complex corrosion processes occurring in the structural materials used in these industries [3, 4]. Hot corrosion is initiated when any metal/alloy surface comes in contact

with heat and an aggressive environment (liquid, solid, and gaseous phases) [5]. In the power industry, low-grade economic fuel (oil, gas) after combustion generates numerous impurities like Na, Cl, S, and V, which in turn produce certain alkali, alkaline sulphates, oxides, and compounds. These compounds combine to form low melting eutectics during combustion, which initiates the hot corrosion process [6]. In general, sulphur, sodium, and vanadium form Na₂SO₄ and V₂O₅ alkali compounds, which get condensed on the surface of the structural parts of the industries. Further, the chemical reaction between Na₂SO₄ and V₂O₅ forms low melting sodium vanadates NaVO₃, which is highly corrosive due to its acidic nature [7, 8]. Thus, metals and alloys (boiler, reheater, superheater) in the combustion system are exposed to an aggressive environment under the presence of flue gases O₂, SO₂/SO₃, and CO₂. Hot corrosion may proceed in two basic steps, i.e. initiation reaction and propagation reaction [9]. The initiation reaction starts after the absorption of gas on the metal surface resulting in the formation of the oxide layer. The oxide layer isolates the underlying surface from the aggressive environment [10]. At this point, the reaction continues through the

✉ Harkulvinder Singh
harkulvinder0081@gmail.com

¹ Yadavindra Department of Engineering, Punjabi University
Guru Kashi Campus, Talwandi Sabo, Punjab 151302, India

² Maharaja Ranjit Singh Punjab Technical University,
Bathinda, Punjab 151001, India

solid-state diffusion by reactants forming a low melting point eutectic mixture and covering the surface with a thin film of fused salt [11]. The fused salts create basic fluxing and acidic fluxing mechanisms depending upon the nature of oxides with oxygen anions. The protection of the oxide layer compromises basic fluxing in the initiation stage after combining oxides with O^{2-} to form anions. At the same time, basic fluxing of oxides transforms into acidic fluxing in the propagation stage after the decomposition of oxides into corresponding cations and O^{2-} anions [12, 13]. Metal degradation starts rapidly in the propagation reaction due to the acidic nature of the deposit salts [14]. Moreover, the HTC degradation of metals /alloys depends on the component's temperature. According to the range of temperature, HTC is further subdivided into two categories, namely low-temperature hot corrosion (LTHC) and high-temperature hot corrosion (HTHC). The low-temperature hot corrosion takes place in the range of 600–750 °C, and high-temperature hot corrosion takes place in the range of 800–950 °C [15, 16]. HTC reduces the overall efficiency and lifetime of working components, resulting in frequent component repair, cost of maintenance, and industry downtime, all of which lead to huge economic losses. To combat all such massive economic failures in industrial applications, the degradation of components due to hot corrosion must be remedied [17].

Techniques for preventing and controlling hot corrosion include the appropriate selection of superalloy, protective coatings, and cathodic protection [18]. Superalloys cannot be immune to hot corrosion attacks indefinitely, although there are some alloy compositions that require a long initiation time before the hot corrosion process moves from the initiation stage to the propagation stage [19, 20]. From the group of corrosion protection techniques, thermal spray coating is the most effective technique that extends the life span of the industrial material by defending them against corrosion, corrosion–erosion, and wear [21]. Presently, several thermal spray coating processes are used, namely plasma arc spray, high-velocity oxy-fuel, detonation gun, wire arc, cold spray, etc. Researchers are interested in HVOF (high-velocity oxygen fuel) cermet coatings because of the advantages of HVOF spraying with a relatively low flame flow temperature (about 3000 °C), high powder flight speed, low decomposition rate, low porosity, and strong bonding strength [22–24].

Currently, the Cr_3C_2 –NiCr coating is one of the most successful cermet coatings and is widely used for high-temperature corrosion, erosion–corrosion, and wear protection due to its high thermal stability, microhardness, lower surface roughness, and lower microporosity [25]. Various authors [26–29] compared the performance of HVOF-sprayed Stellite-6, Ni-20Cr, Cr_3C_2 –25NiCr, and NiCrBSi coatings on various superalloys after subjecting

to a Na_2SO_4 – V_2O_5 salt environment at 900 °C. The authors observed that all the coated superalloys provide better corrosion resistance to the base material. In contrast, Ni-20Cr coatings performed better than their counterparts due to the formation of Ni and Cr oxides and spinels that provide resistance to HTC. Bhatia et al. [30] investigated the hot corrosion of T-91 steel at different temperatures (550, 700, and 850 °C) for 50 cycles after depositing Cr_3C_2 –25%(Ni-20Cr) coating with the HVOF gun. The results indicated that the formation of Cr_2O_3 , along with NiO and $NiCr_2O_4$ phases, protected up to 700 °C after that (850 °C) coating failed due to penetration of molten salt (Na_2SO_4 – V_2O_5) species. Baiamonte et al., [31] examined the hot corrosion resistance of HVOF-sprayed Cr_3C_2 –25%NiCr, Cr_3C_2 –25%CoNiCrAlY, and SiO_2 (nano) + mullite 60% (Al_2O_3 – SiO_2) coatings in as-sprayed and post-treated (laser) conditions under the mixture of Na_2SO_4 + 60% V_2O_5 at 700 °C, for 50 h, 100 h, and 200 h, respectively. Authors reported that post-treated (laser) Cr_3C_2 –NiCr coating reduced the overall material consumption rate as compared to its counterparts, which may attribute to the oxides of Cr_2O_3 , Cr_3C_2 , and Ni as revealed by XRD results. Shi et al. [32] explored the hot corrosion performance of HVOF deposited Cr_3C_2 –NiCr–NiCrAlY coating under the Na_2SO_4 environment at 750 °C, 800 °C, and 900 °C. The combination of Cr_3C_2 –NiCr–NiCrAlY coating exhibited good resistance to Na_2SO_4 hot corrosion at 750 °C, mainly because of the dense Cr_2O_3 scale that slowed down further corrosion attack. The above combination of coatings shows longitudinal cracks in the temperature range of 800 °C and 900 °C. Authors [33–36] explored the hot corrosion resistance of Cr_3C_2 –NiCr coatings deposited with HVOF and APS spraying guns on various boiler tube steels (T-22, 304SS, and alloy 80A) in the presence of Na_2SO_4 + 60% V_2O_5 salt in the temperature range of 800–950 °C for 50 cycles. The superior hot corrosion resistance was obtained due to the formation of oxide layers consisting of Cr_2O_3 , Cr_2O_4 , NiO, and $NiCr_2O_4$ phases. From the comparison point of view, the HVOF-coated substrates represent better protection than the APS process. The uncoated specimen degrades at a faster rate than the coated samples. Moreover, the Cr_3C_2 –25%NiCr-coated steels performed better at 800 °C as compared to 900 °C and 950 °C. From the literature, it is concluded that the thermal stability of the Cr_3C_2 –NiCr coating gets affected in the presence of a molten salt environment. Molten salt's role as an oxygen carrier encourages the penetration of corroding species, lowering the barrier to hot corrosion. Generally, Cr_3C_2 –NiCr coating provides better protection in an aggressive environment due to the combination of carbide phase (Cr_3C_2) and metallic binder phase (NiCr). Besides the mechanical, microstructural, and chemically stable properties (creep, fatigue, microhardness, microporosity,

Table 1 Actual composition (Wt.%) for “TP347H” boiler tube steel used in present study

Element	Cr	Ni	C	Mn	P	S	Si	Nb	Fe
Wt.%	17.53	11.42	0.067	1.54	0.024	0.001	0.59	0.70	Bal

wear, oxidation, etc.), oxide scale dissolution and cracking/spallation resistance in the molten salt are equally essential for successful operation at high temperatures. Although conventional coating provides protection to the base material, the oxide scale may dissolve (acidic reaction) or crack (residual stresses) at high temperatures [37].

Many reports explored that the doping of rare earth elements (RE) in the coatings can further improve the microstructure, enhancing coating stability in front of HTC attack [38, 39]. Studies reported by various researchers [40–42] show that RE elements (Y, Zr, La, Gd, Dy, and Ce) can improve the coating microstructure by refining grain size, adhesion strength, plasticity, stress-relieving, and oxide growth rate, pegging formation and chemical stability. From the above addressed RE elements, the cerium/cerium oxide (lanthanide) has a unique property to store and release oxygen when subjected to high temperature [43]. Due to this characteristic, it is used in various applications such as automobile catalytic converts, biomedical implants, solid fuel cells, polishing compounds, and high-temperature coatings [44]. This research, therefore, has been conducted to elucidate the role of CeO₂ particles on the hot corrosion behaviour of TP347H steel after blending in Cr₃C₂–NiCr coating with different fractions ((0.4 wt.%, 0.8 wt.%, and 1.2 wt.%) and the result can provide some valuable information to utilize in enhancing the life of power plant boiler components. Moreover, the influence of ceria on coatings microstructural changes is characterized using basic analysis techniques. Furthermore, the effect of three ratios of ceria on oxide scale thickness is also observed after the hot corrosion study.

2 Materials and Methods

For the current research experiment, ASTM-A312 grade TP347H austenite steel had been selected as substrate material, which is widely used in boiler superheater, reheater, and heat exchanger tubes. The tube of 55 mm diameter was taken from Guru Nanak Dev Thermal Plant, Bathinda, Punjab (India). The chemical composition of substrate steel was analysed with X-ray fluorescence spectroscopy (XRF), which is reported in Table 1. The samples of 20 mm × 15 mm × 5 mm were cut from a fresh tube with a wire cut EDM and polished with emery papers (220 μm to 800 μm). The chemical composition and designations of the feedstock powders after homogeneous blending with jar milling are reported in Table 2. All samples were grit blasted

Table 2 Designation used for each specimen during present study

Specimens	Nomenclature
1. 75Cr ₃ C ₂ –25NiCr	HS
2. 75Cr ₃ C ₂ –25NiCr + 0.4 wt.%CeO ₂	HS1
3. 75Cr ₃ C ₂ –25NiCr + 0.8 wt.%CeO ₂	HS3
4. 75Cr ₃ C ₂ –25NiCr + 1.2 wt.%CeO ₂	HS5

Table 3 Spray parameters employed for HVOF coating (HIPOJET 2700)

Parameter	Value
Oxygen flow rate	200 SLPM
Fuel (LPG) flow rate	50 SLPM
Air-flow rate	900 SLPM
Spray distance	200 mm
Powder feed rate	38–40 g/min
Fuel pressure	6.00 kg/cm ²
Oxygen pressure	8.00 kg/cm ²
Air pressure	6.00 kg/cm ²
Flame temperature	1900–2200 °C

SLPM standard litre per minute

with alumina powder before coatings were applied using a high-velocity oxy-fuel (HVOF) gun provided by Metallizing Equipment Pvt. Ltd. Jodhpur (Rajasthan). The various technical parameters of HVOF spraying are listed in Table 3. Around 220–290-μm-thick coatings were formulated on the TP347H steel. The as-coated samples were characterized using JEOL-7610Plus, Japan, with EDS genesis software and an X-rays diffractometer (Bruker AXS D-8, Germany) to evaluate the surface microstructure and phase compositions of alloy powder. The coating powder morphology (SEM/EDS) for Cr₃C₂–NiCr and CeO₂-blended Cr₃C₂–NiCr powders is shown in Fig. 1a and Fig. 1b, respectively. The surface characterization results (SEM/EDS) of as-deposited coatings are depicted in Figs. 2, 3, 4, and 5. The surface roughness, microporosity, and microhardness results of the as-deposited coatings are reported in Table 4.

2.1 Coating Characterization

The surface characterization results of as-deposited coatings are depicted in Figs. 2, 3, 4, and 5. The conventional carbide coating (HS) indicates the major phases of Cr₃C₂, Cr, and Ni. In contrast, ceria-modified chromium carbide

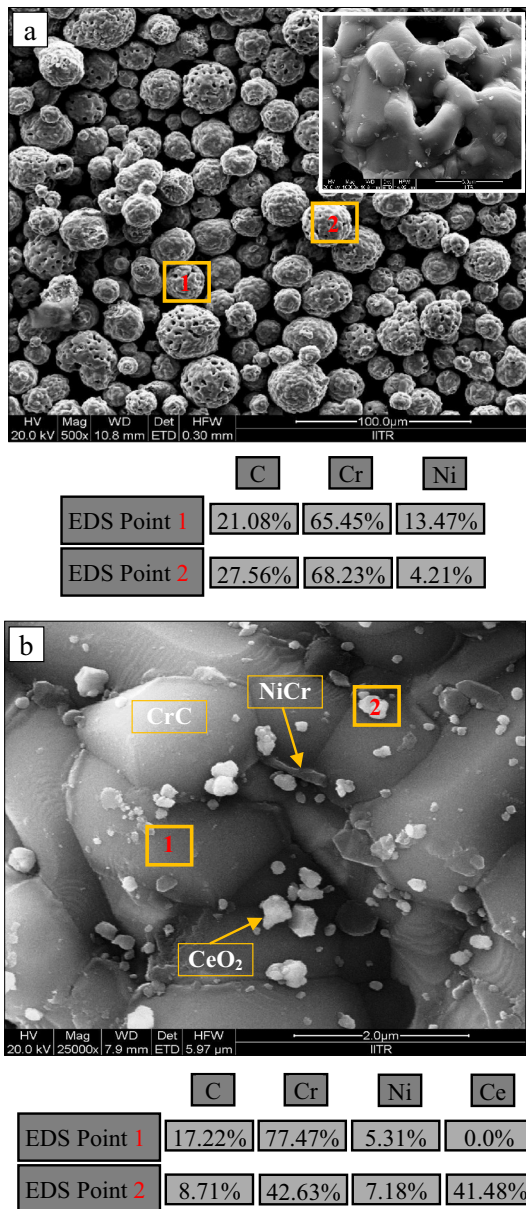


Fig. 1 FESEM micrograph of coating powders **a** Cr₃C₂-NiCr powder with EDS analysis **b** CeO₂ (1.2 wt.%) doped Cr₃C₂-NiCr powder with EDS analysis

coatings (HS1, HS3, and HS5) show the presence of significant phases of Cr₃C₂, Cr, and Ni, along with CeO₂. The coating surface shows the typical characteristics, i.e. the homogeneous microstructure of spread molten droplets, a visual interface between solidified melted, partially melted, and unmelted particles without cracks and inclusions. The unmelted particles on the coating's surface were reduced (Fig. 3b) after adding a rare earth element in a lower concentration (0.4 wt-% CeO₂) to the chromium carbide powder. As the concentration of cerium increased to 0.8 wt-%, it increased the amount of unmelted particles, as can be seen

in Fig. 4b. Furthermore, the amount of unmelted particles increased (Fig. 5b) with a higher concentration of (1.2 wt-%) of ceria in the Cr₃C₂-NiCr coating as compared to its counterparts. The dark grey colour shows the presence of (Cr₃C₂) carbides with NiCr binder (light grey). Traces of CeO₂ (white colour) were also observed on the HS1, HS3, and HS5 coatings surface, which is confirmed by EDS results, as indicated in Figs. 3b, 4b, and 5b, respectively.

2.2 Hot Corrosion Studies

The PID controller kept the temperature of the furnace at 750 °C. Ceramic boats were utilized to place the samples in the furnace to carry out corrosion studies. All the samples were cleaned with acetone, and a prepared salt mixture of Na₂SO₄-60%V₂O₅ was applied in the range of 3–5 mg/cm² using a camel hairbrush. Each sample was placed in an alumina boat, which was then fed into the tube furnace with the assistance of a tong. The sample was allowed to heat in the furnace for 1 h, followed by 20 min of cooling in the air. After every cycle, the weight of the ceramic boat, including the specimen, can be recorded using an electronic weighing machine. Each sample was exposed to a molten salt environment for 50 cycles. Weight gain measurements were used to investigate the kinetics of corrosion, and the scale dislodged from the sample was also included in the weight change data. The surface and x-section of corroded specimens have been analysed by XRD, SEM/EDS, and mapping techniques.

3 Results

3.1 Visual Examination

Figure 6 shows the surface morphologies of bare and HVOF-coated samples after exposure to an aggressive environment of molten salt (Na₂SO₄-60%V₂O₅) at 750 °C inside the heating zone of the furnace for 50 cycles. For uncoated TP347H steel (Fig. 6a), the scale formation was noticed at the end of the 4th cycle with rusty patches, and swelling of the scale was observed by the 20th cycle during experimentation. The bare steel developed surface cracks by the end of the 34th cycle. During the cyclic study, TP347H steel shows scale cracking and spallation. In the case of HS-coated (Fig. 6b) steel, the colour of the sample turned greenish-black from silver-grey after the 5th cycle, and minor spallation (on the edges) appeared in the coating after the 43rd cycle. Ceria-modified HS1-coated steel only showed colour change with the greenish tone and minor rusty patches after the third cycle, which remained present throughout the study. No scale spallation was observed for the HS1-coated steel, as shown in Fig. 6c. Similarly, ceria-modified HS3- and HS5-coated steel (Figs. 6d, e) experienced a change in colour

Fig. 2 Surface SEM/EDS analysis of the HVOF as-sprayed **a** Cr₃C₂-NiCr-coated TP347H steel at ×500 magnification, and **b** Cr₃C₂-NiCr-coated TP347H steel at ×10,000 magnification

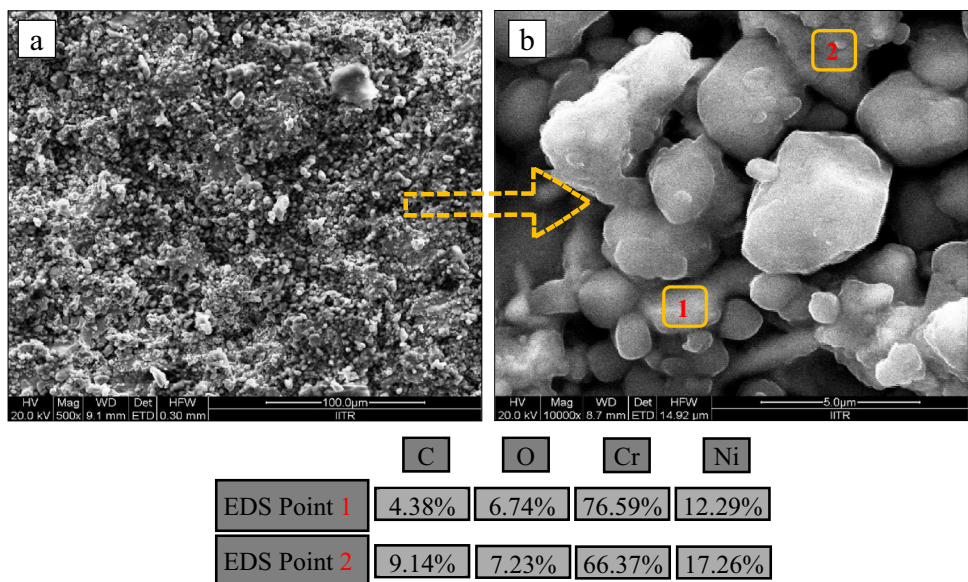
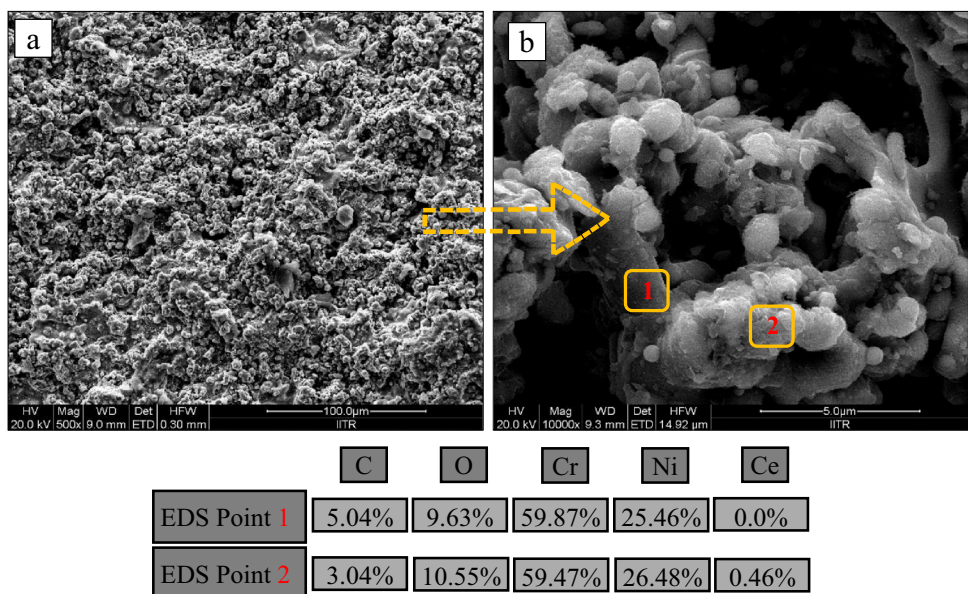


Fig. 3 Surface SEM/EDS analysis of the HVOF as-sprayed **a** 0.4 wt.% + Cr₃C₂-NiCr-coated TP347H steel at ×500 magnification, and **b** 0.4 wt.% + Cr₃C₂-NiCr-coated TP347H steel at ×10,000 magnification



from light grey to dark blackish tone after the fifth and third cycles. In the case of HS5-coated steels, minor spallation (on edge) of the oxide scale was observed after the 35th cycle, whereas HS3-coated steel was free from any spallation, as shown in Fig. 6e.

3.2 Weight Gain Analysis

Figure 7 shows the weight gain bar chart for bare and HVOF-coated samples after subjecting to an aggressive environment of Na₂SO₄-60%V₂O₅ salt at 750 °C for 50 cycles. HS1-coated steel shows minor weight gain (2.434 mg/cm²) as compared to its counterparts. Rare earth (RE) element (Ce) in the conventional coating acts as nucleation sites for

the oxide layer, which reduces the distance of neighbouring oxide grains, resulting in a smaller oxide gain size. Subsequently, the protective oxide layer developed in a shorter time, which helps in achieving rapid steady-state conditions and allows minor weight gain [45, 46]. The minor weight gain shows the protective nature of the coating. The bare TP347H steel gained a weight of 12.381 mg/cm² during the experiment, which might be due to a massive amount of oxygen diffusion (including corroded species) towards the steel substrate. In the case of bare steel, some of the oxide scale sputtered outside the alumina, which might be due to the excessive thermal stresses developed in the oxide scale during the cooling cycle. From the HVOF-coated steel, the HS sample provided the least protection with a mass

Fig. 4 Surface SEM/EDS analysis of the HVOF as-sprayed **a** 0.8 wt.% + Cr₃C₂-NiCr-coated TP347H steel at ×500 magnification, and **b** 0.8 wt.% + Cr₃C₂-NiCr-coated TP347H steel at ×10,000 magnification

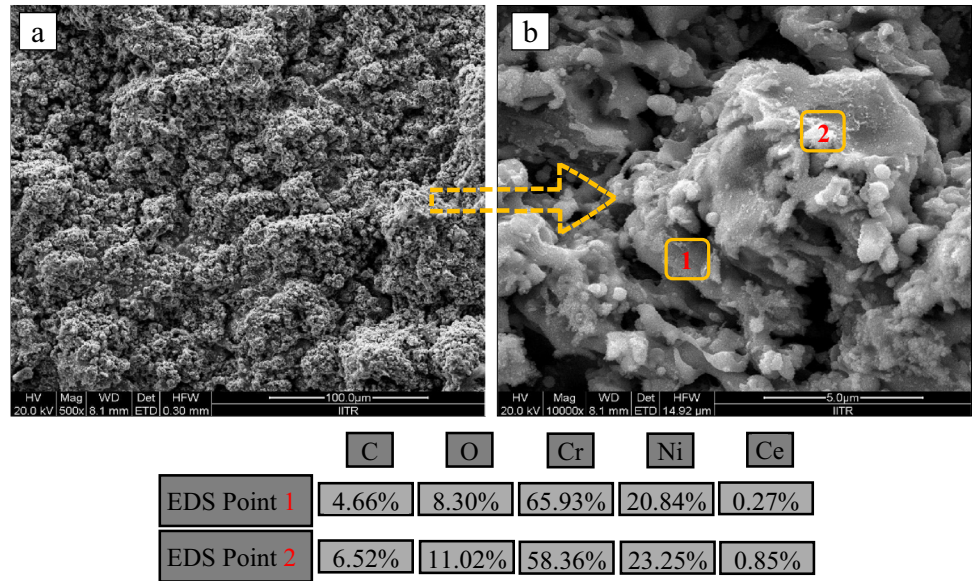


Fig. 5 Surface SEM/EDS analysis of the HVOF as-sprayed **a** 1.2 wt.% + Cr₃C₂-NiCr-coated TP347H steel at ×500 magnification, and **b** 1.2 wt.% + Cr₃C₂-NiCr-coated TP347H steel at ×10,000 magnification

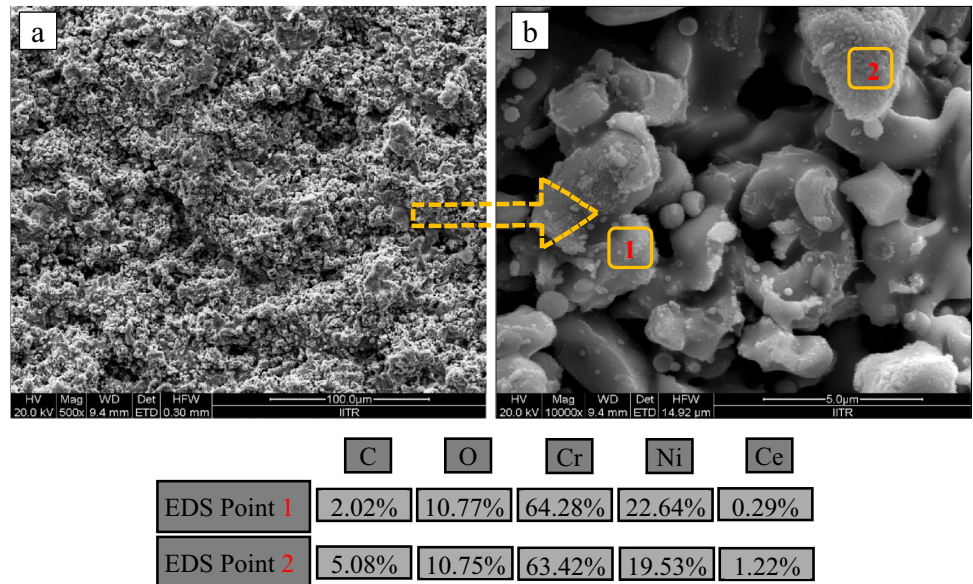


Table 4 Coating composition; microhardness, porosity, and surface roughness

Coatings	Microhardness (Hv)	Porosity (%age)	Surface Roughness (µm)
1. 75Cr ₃ C ₂ -25NiCr	805.4	<1.8%	5.792
2. 75Cr ₃ C ₂ -25NiCr+0.4 wt.% CeO ₂	813.0	<1%	4.832
3. 75Cr ₃ C ₂ -25NiCr+0.8 wt.% CeO ₂	840.9	<1.2%	4.648
4. 75Cr ₃ C ₂ -25NiCr+1.2 wt.% CeO ₂	887.2	<1.5%	4.314

gain of 10.865 mg/cm². HS3 and HS5 coatings provided good protection to the base material, with a weight gain of 5.936 mg/cm² and 9.011 mg/cm², respectively. Figure 7 depicts the benefit of ceria addition in conventional coating

for combating hot corrosion attacks in a molten salt environment. The weight gain bar chart illustrates that the minimum quantity of ceria (0.4 wt.%) added Cr₃C₂-NiCr coating (HS1) provided maximum resistance to hot corrosion,

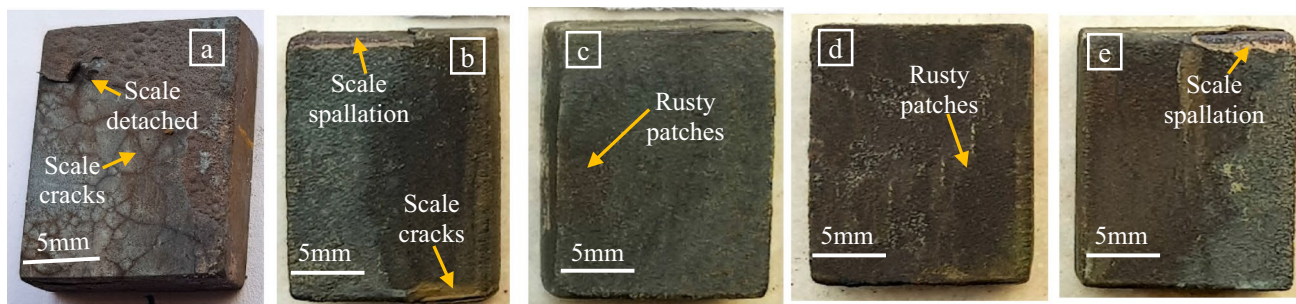


Fig. 6 Micrographs of **a** bare TP347H steel, and HVOF-sprayed **b** Cr_3C_2 -NiCr-coated **c** Cr_3C_2 -NiCr+0.4 wt.% CeO_2 -coated **d** Cr_3C_2 -NiCr+0.8 wt.% CeO_2 -coated, and **e** Cr_3C_2 -NiCr+1.2 wt.%

CeO_2 -coated TP347H steel after subjecting to Na_2SO_4 - V_2O_5 salt environment at 750 °C for 50 cycles

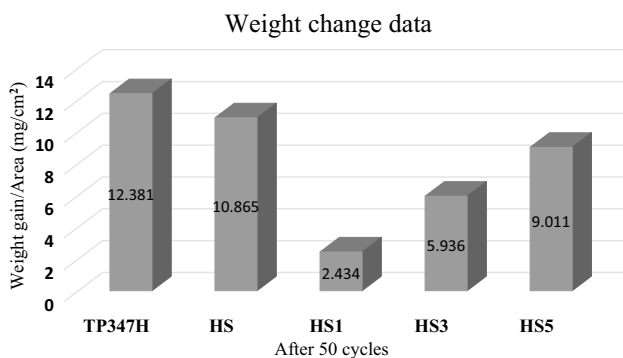


Fig. 7 Weight gain bar chart of **a** bare TP347H steel, and HVOF-sprayed **b** Cr_3C_2 -NiCr-coated **c** Cr_3C_2 -NiCr+0.4 wt.% CeO_2 -coated **d** Cr_3C_2 -NiCr+0.8 wt.% CeO_2 -coated, and **e** Cr_3C_2 -NiCr+1.2 wt.% CeO_2 -coated TP347H steel after subjecting to Na_2SO_4 - V_2O_5 salt environment at 750 °C for 50 cycles

followed by HS3 (ceria 0.8 wt.% added Cr_3C_2 -NiCr), HS5 (ceria 1.2 wt.% added Cr_3C_2 -NiCr), and HS (Cr_3C_2 -NiCr) coating. As the concentration of CeO_2 increases in the carbide coating, the performance of the ceria-doped coating decreases. A higher concentration of ceria (0.8 wt.% and 1.2 wt.%) results in more number of nucleation sites; hence, HS3- and HS5-coated samples attained higher weight.

3.3 XRD Analysis

Spectrums of the X-ray diffraction study for corroded bare and HVOF-coated TP347H steel are revealed in Fig. 8. The uncoated TP347H sample indicates (Fig. 8a) the existence of Fe_2O_3 and Fe_3O_4 scale throughout its surface along with NiFe_2O_4 , NiCr_2O_4 , $\text{Ni}(\text{VO}_3)_2$, and NaFeO_2 after being exposed to a highly hostile molten salt NaVO_3 and Na_2SO_4 phases at 750 °C for 50 h under cyclic conditions. It can be inferred that due to the formation of the above phases, uncoated steel weight increases continuously during the study. After undergoing XRD analysis (Fig. 8 b),

the peaks generated while analysing Cr_3C_2 -NiCr-coated (HS) TP347H steel confirmed the presence of Cr_2O_3 , Cr_{23}C_6 , Cr_7C_3 , NiO, and NiCr_2O_4 along with NaVO_3 and $\text{Na}_2\text{V}_2\text{O}_5$ phases. The molten salt species (Na, S, and V) react with each other at high temperatures in the presence of oxygen to form various complex compounds, as seen in Fig. 8. These complex compounds further penetrate/diffuse through porosity and dissolve the protective layer of oxides, reducing the hot corrosion resistance of the deposited coatings, as shown in Fig. 9d. All the ceria-doped Cr_3C_2 -NiCr coatings (HS1, HS3, and HS5) show the common protective phases of Cr_2O_3 , NiCr_2O_4 , and CeCrO_3 , along with NaVO_3 - and Na_2SO_4 -corroded species as illustrated by Fig. 8c–e. HS3- and HS5-corroded samples show one more common phase of Ce_2O_3 during the XRD analysis. Various researchers [47–49] have reported the protective nature of Cr_2O_3 , Cr_{23}C_6 , Cr_7C_3 , NiCr_2O_4 , CeCrO_3 , and Ce_2O_3 compounds.

3.4 Surface Analysis

The morphology of the coated and uncoated samples and the structure of elements existing at certain points on their surface after exposure to a molten salt environment at 750 °C for 50 cycles is depicted in Figs. 9, 10, and 11, respectively. The EDS analysis of uncoated steel (Fig. 9a, b) shows the scale mainly consisted of Fe and O, along with Cr and Ni. The molten salt corroding species Na and V were also identified by the surface EDS analysis. At higher magnification, bare TP347H steel shows a plate-like structure after the reaction of molten salt and basic constituents of the steel. The conventional carbide coating (HS) does not provide adequate protection with Cr and Ni, as illustrated by the surface SEM (Fig. 9c, d). The HS-coated steel sample indicates a crack on the surface (Fig. 9c, d); it may be due to the presence of Na and V salt species as detected by the EDS study. Ceria-modified carbide coatings (HS1 and HS3) successfully protected the substrate steel with oxides of Cr, Ni, and

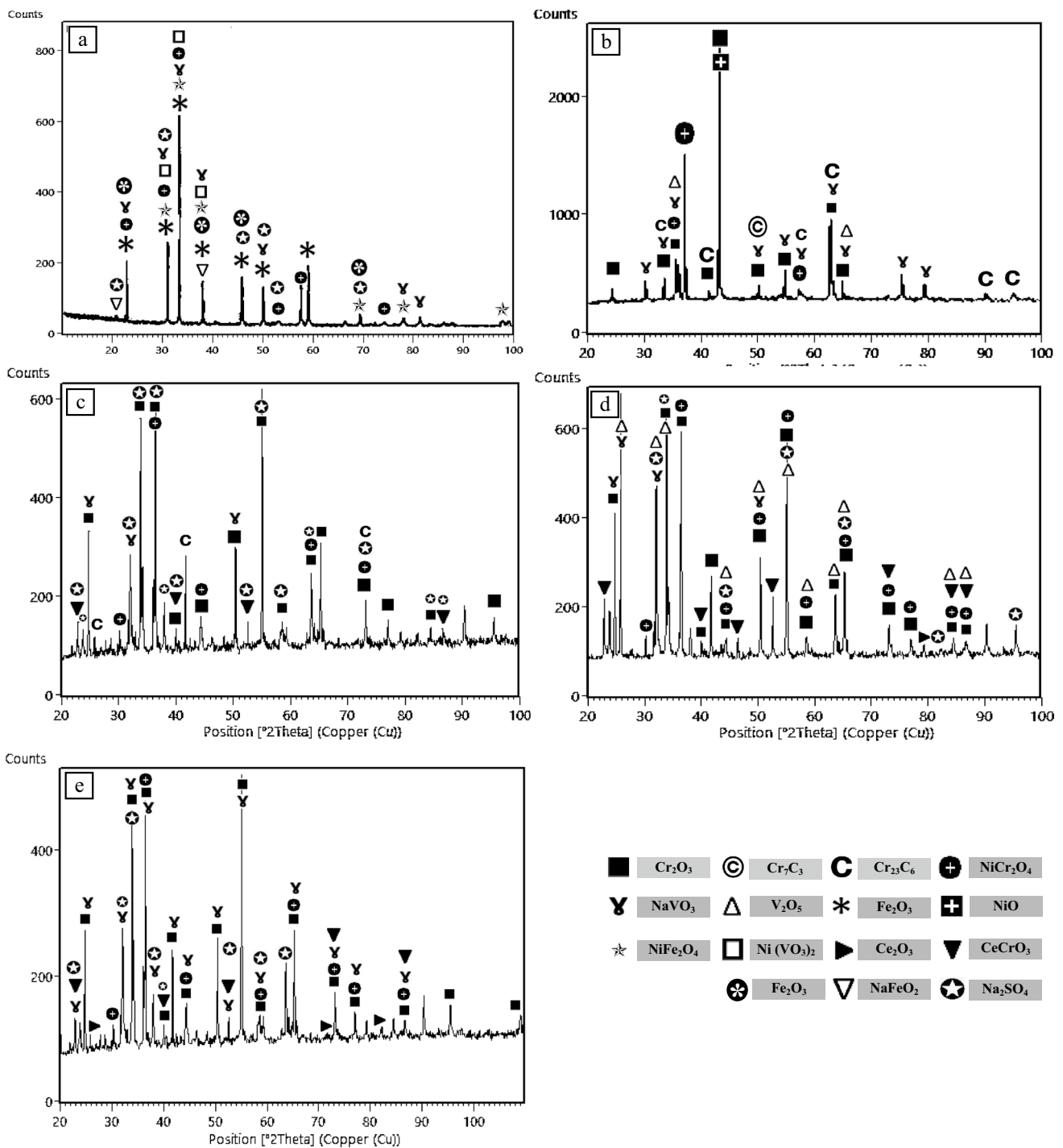


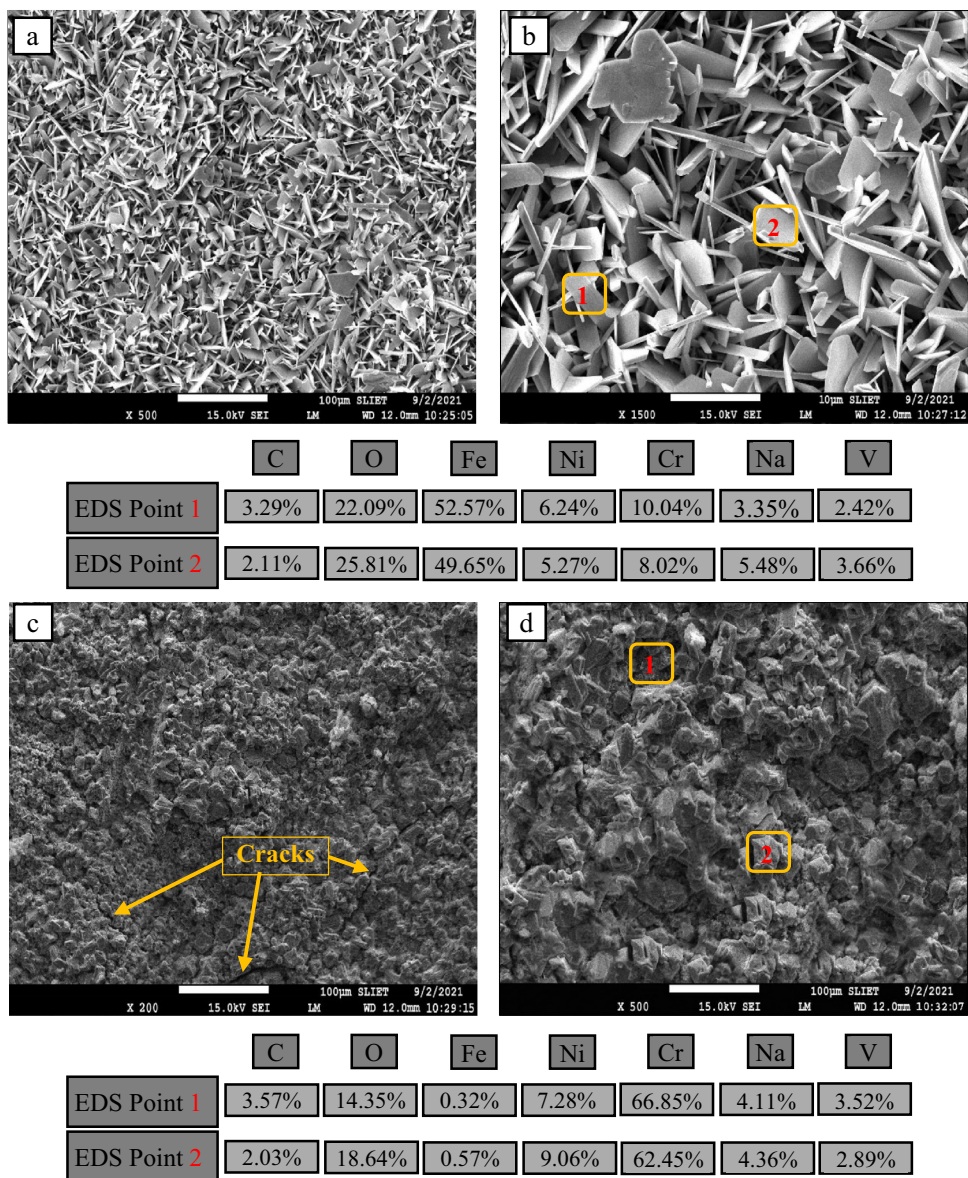
Fig. 8 XRD spectra of **a** bare TP347H steel, and HVOF-sprayed **b** Cr₃C₂-NiCr-coated **c** Cr₃C₂-NiCr+0.4 wt.% CeO₂-coated **d** Cr₃C₂-NiCr+0.8 wt.% CeO₂-coated, and **e** Cr₃C₂-NiCr+1.2 wt.%

CeO₂-coated TP347H steel after subjected to Na₂SO₄-V₂O₅ salt environment at 750 °C for 50 cycles

Ce, as revealed in the SEM/EDS study (Fig. 10). There is no crack observed during the surface analysis, as shown in Fig. 10, which might be due to the lower wt.% of ceria doped in Cr₃C₂-NiCr coating. Various authors [50–52] reported the beneficial results of RE elements when doped

in a lower concentration. Figure 11a shows a crack on the surface of coated steel after subjected to the molten salt environment. The surface SEM/EDS study reveals the Cr and Ni along with oxygen as major elements and Ce, Na, V, and S as minor elements. In this case, ceria-coated

Fig. 9 Surface SEM/EDS analysis of **a** bare TP347H steel at magnification of $\times 500$ **b** bare TP347H steel at magnification of $\times 1500$ **c** Cr₃C₂-NiCr-coated TP347H steel at magnification of $\times 200$ **d** Cr₃C₂-NiCr-coated TP347H steel at magnification of $\times 500$ after subjecting to Na₂SO₄-V₂O₅ salt environment at 750 °C for 50 cycles



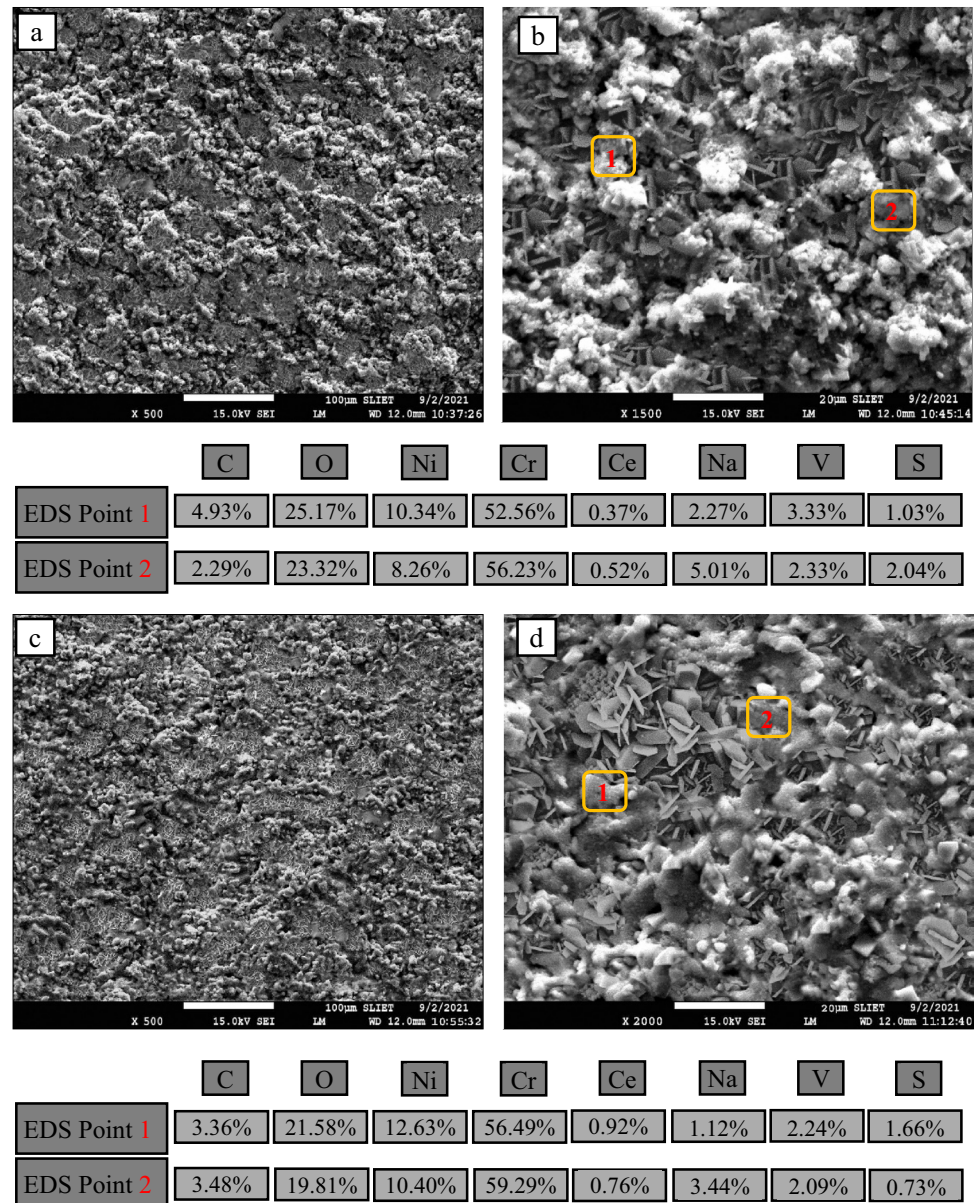
(HS5) steel shows partial protection to the substrate material, which might be due to the higher concentration (1.2 wt.% Ce) of RE element in the carbide coating.

3.5 Cross-Sectional SEM/EDS Study

Figure 12 depicts the SEM/EDS point analysis of the corroded bare and HVOF-coated steel after subjecting to a molten salt corrosion environment at 750 °C for 50 cycles. The bare TP347H steel substrate experienced a corrosion attack as iron (Fe) diffused from the base metal (Point 1) to the top surface (Point 6), as shown in Fig. 12a. Molten salt contaminants such as Na, V, and oxygen travel towards the substrate surface, which is mainly responsible for hot corrosion attacks. HS coating provided inadequate protection due to the penetration

of the molten salt towards the oxide scale, reducing its capability to resist hot corrosion attacks. The EDS points 6, 7, and 8 confirm Na and V presence near the coating surface after consuming the thick protective oxide scale, as shown in Fig. 12b. Dissolution (basic fluxing) of the protective oxide scale was observed during the hot corrosion study, which might be due to the acidic nature of the NaVO₃ salt phase. Corroding species consumed the protective oxide layer during the propagation stage of hot corrosion. Ceria-doped (0.4 wt.%) carbide coating (HS1) provided excellent hot corrosion resistance, as evident by points 6 and 7 EDS analysis (Fig. 12c). The concentration of Cr and Ni at points 6 and 7 is decreased as compared to the HS-coated sample, which might be due to the presence of Ce in the HS1-coated steel. Compact

Fig. 10 Surface SEM/EDS analysis of $\text{Cr}_3\text{C}_2\text{-NiCr} + \text{CeO}_2$ (0.4 wt.%) -coated TP347H steel at **a** 500 \times , and **b** 1500 \times magnification, and surface SEM/EDS analysis of $\text{Cr}_3\text{C}_2\text{-NiCr} + \text{CeO}_2$ (0.8 wt.%) -coated TP347H steel at **c** 500 \times , and **d** 1500 \times magnification after subjecting to $\text{Na}_2\text{SO}_4\text{-V}_2\text{O}_5$ salt environment at 750 °C for 50 cycles



oxide scale of Cr and Ni along with Ce is observed in Fig. 12c.

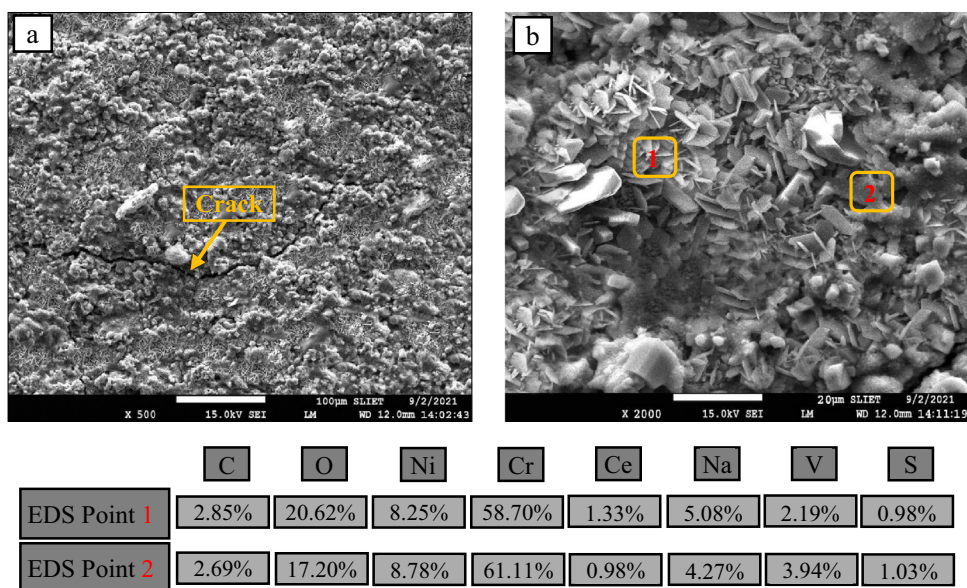
In contrast, HS3-coated steel shows higher values of Cr and Ni at points 6, 7, and 8 than the HS1 sample but lower than that of HS-coated steel. No diffusion of oxygen and corroding species (Na, V, and S) was noticed, which is confirmed from points 4 and 5 in Fig. 12d. Points 2–5 show only the basic composition of the feedstock powder (Cr, Ni) coating. In this case, ceria with a ratio of 0.8 wt% in $\text{Cr}_3\text{C}_2\text{-NiCr}$ coating provided good protection to the substrate steel. As the ceria (1.2 wt%) ratio increases in the conventional carbide coating, it loses its capability to provide a compact and smooth oxide scale, as shown in Fig. 12e. EDS points 6, 7, and 8 show the higher concentration of

Cr, Ni, and Ce, which indicates the possibility of oxides of these elements.

3.6 X-rays Mapping

The X-ray mapping results for the bare and HVOF-coated samples after 50 cycles under the molten salt atmosphere at 750 °C are depicted in Figs. 13 and 14. Figure 13a shows the hot corrosion attack of molten salt species (Na, V) on the TP347 steel surface. Substrate elements (mainly Fe, Cr, and Ni) diffused towards the bare steel surface, which is validated by the X-ray mapping results. HVOF-coated (HS) steel shows a thick oxide scale of Cr along with Ni spinels, which enhances the hot corrosion stability of the coating. However, the protection of the coating decreases in

Fig. 11 Surface SEM/EDS analysis of **a** Cr₃C₂-NiCr+CeO₂ (1.2 wt.%) coated TP347H steel at magnification of ×500 **b** Cr₃C₂-NiCr+CeO₂ (1.2 wt.%) coated TP347H steel at magnification of ×2000 after subjecting to Na₂SO₄-V₂O₅ salt environment at 750 °C for 50 cycles



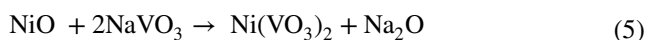
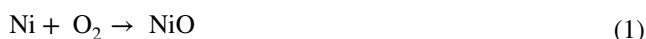
the presence of molten salt, i.e. Na and V, as illustrated in Fig. 13b. The protective oxide layer may dissolve in the presence of molten salt after the combined reaction of Na and V to form NaVO₃, as identified by XRD analysis (Fig. 8b). Ceria-doped Cr₃C₂-NiCr coatings (HS1, HS3) successfully enhanced the hot corrosion resistance, as illustrated by mapping analysis (Fig. 14a, b). In the case of HS1-coated steel (Fig. 14a), the ceria map confirms the role of the RE element as the concentration of Cr and Ni is minimum as compared to its counterparts. There is no diffusion of corroding contaminants (Na, V, and S) that took place, which was successfully retarded by the dense scale of Cr and spinels of Ni along with Ce. The map study Fig. 14a represents the molten salt present on the surface of the oxide scale, which might be due to the lower porosity of the coating and the steady state of oxidation achieved by the coated steel in a shorter time, which gives very limited time to the corroding elements ingress towards coating. The above improvement has occurred in the presence of lower Wt.% of Ce element.

In comparison with HS1-coated steel, HS3-coated steel provided lower protection to the base material after it gained a higher weight (Fig. 7). The map analysis Fig. 14b illustrates that the thin oxide scale consists of Cr and Ni along with Ce element, which is distributed throughout the coating. No diffusion of corroding elements was observed during the hot corrosion study. As the concentration (0.8 wt.%) of Ce element increased in the Cr₃C₂-NiCr coating (HS3), it increased the amount of Cr towards the oxide scale, as shown in the map results. The map study Fig. 14c for HS5-coated steel illustrated that molten salt species dissolve the protective oxide scale of Cr and Ni along with Ce. In this case, Cr₃C₂-NiCr coating with high wt. ratio of CeO₂ gains more weight as compared to conventional (HS) and

ceria-modified (HS1 and HS3) coatings, which might be due to the higher concentration of RE element.

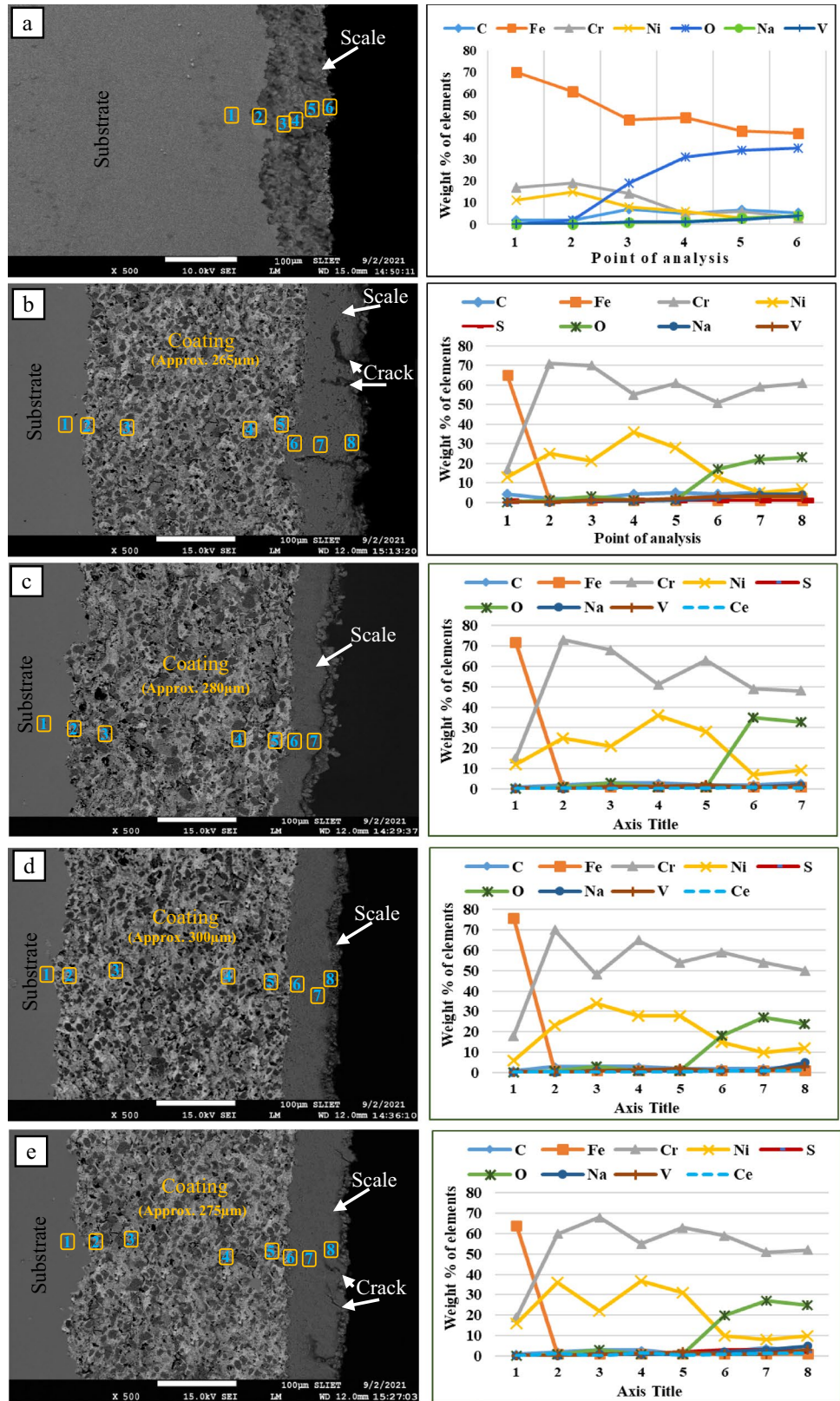
4 Discussion

The bare steel showed rapid inward diffusion of oxygen and outward migration of metal ions takes place during hot corrosion. The metallic ions diffusion creates porous oxide scale composed Fe₂O₃ (hematite) and Fe₃O₄ (Magnetite), phases, along with NaFeO₂, NiFe₂O₄, NiCr₂O₄, and Ni(VO₃)₂ in the presence of melted NaVO₃, which is the product of Na₂SO₄ and V₂O₅ salt after reaction at 750 °C. Above developed phases formed after the complex chemical reactions as follows [53–56].



From the above reactions, the highest weight percentage of iron (52.57% and 49.65%) was observed in surface EDS analysis, as depicted in Fig. 9b, which is further validated by the XRD profile in Fig. 8a. The Fe₂O₃ scale is reported

Fig. 12 Surface SEM/EDS analysis of **a** bare TP347H steel **b** HVOF-sprayed Cr_3C_2 -NiCr-coated steel **c** Cr_3C_2 -NiCr+ CeO_2 (0.4 wt.%) -coated steel **d** Cr_3C_2 -NiCr+ CeO_2 (0.8 wt.%) -coated steel and **e** Cr_3C_2 -NiCr+ CeO_2 (1.2 wt.%) -coated steel after subjecting to Na_2SO_4 - V_2O_5 salt environment at 750 °C for 50 cycles



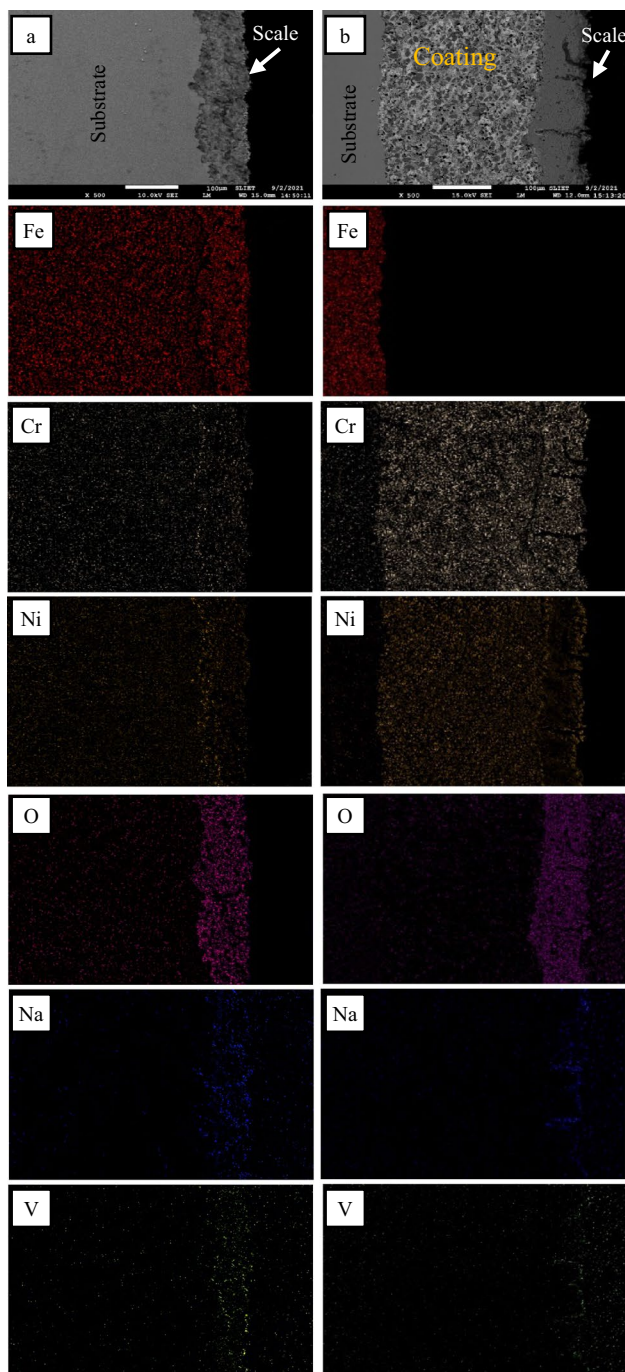
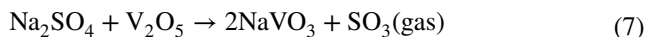


Fig. 13 Mapping analysis of **a** bare TP347H steel and **b** HVOF-sprayed Cr_3C_2 -NiCr-coated TP347H steel after subjecting to Na_2SO_4 - V_2O_5 salt environment at 750 °C for 50 cycles

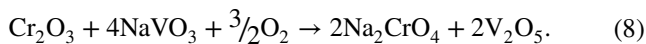
to be porous and unprotective, which could not block the penetration of oxygen and corroding species. Moreover, it affects the stability of NiCr_2O_4 compounds [57]. Figure 6a shows a macrograph with surface cracks of hot corroded bare TP347H steel, which might be due to the stress generated by the continuous formation of new oxides under the

top oxide scale [58]. The formation of $\text{Ni}(\text{VO}_3)_2$ (Ni vanadate) decreases the aggressiveness of the molten salt due to a higher melting point (700 °C) [59]. However, the NaFeO_2 compound may exist after the reaction of Fe and Na in the presence of oxygen, which is non-protective, according to Liu et al., [60]. In the present study bare TP347H steel was continuously consumed after developing non-protective oxides of iron during the hot corrosion study.

The oxide scale formation is also validated by the change in colour of the HS-coated sample from light grey to dark grey (Cr_2O_3) along with dark green (NiO) patches [61]. The molten salt mixture has also been ingressed on the surface of HS-coated steel. Points 1 and 2 on the surface (Fig. 9d) suggest the formation of Cr and Ni oxides, which is further confirmed by the mapping analysis (Fig. 13b). Moreover, the oxides authenticated by XRD results (Fig. 8b) indicate the occurrence of a major phase of Cr_2O_3 and NiO along with Cr_{23}C_6 , Cr_7C_3 , NiCr_2O_4 , and minor phases of NaVO_3 and V_2O_5 . The topmost developed oxide scale of Cr_2O_3 , enhances the hot corrosion protection up to 950 °C [62–65]. In addition, the spinels of Ni and Cr (NiCr_2O_4 —Eq. 4) also facilitated hot corrosion resistance due to their low diffusion coefficient than parental oxides [66]. The thick and protective oxide scale (100 μm) of Cr_2O_3 along with NiCr_2O_4 spinels acted as a barrier to corroding species after sealing the boundaries/paths towards coating [67]. Nevertheless, the presence of NiO in the oxide scale may reduce the stability of the coating due to its porosity (partially), which may allow the oxidizing and corrosive species to reach the coating and substrate, as reported by [68, 69]. However, the oxide scale may dissolve in the propagation stage of hot corrosion in the presence of molten salt, as can be seen in Fig. 12b. Depending upon the salt composition (Na_2SO_4 : V_2O_5), the Cr_2O_3 scale may dissolve in Na_2SO_4 as anionic species (basic fluxing) or cationic species (acid fluxing) [70]. Acidic NaVO_3 compound formed after the reaction between Na_2SO_4 and V_2O_5 via the following reaction [71].

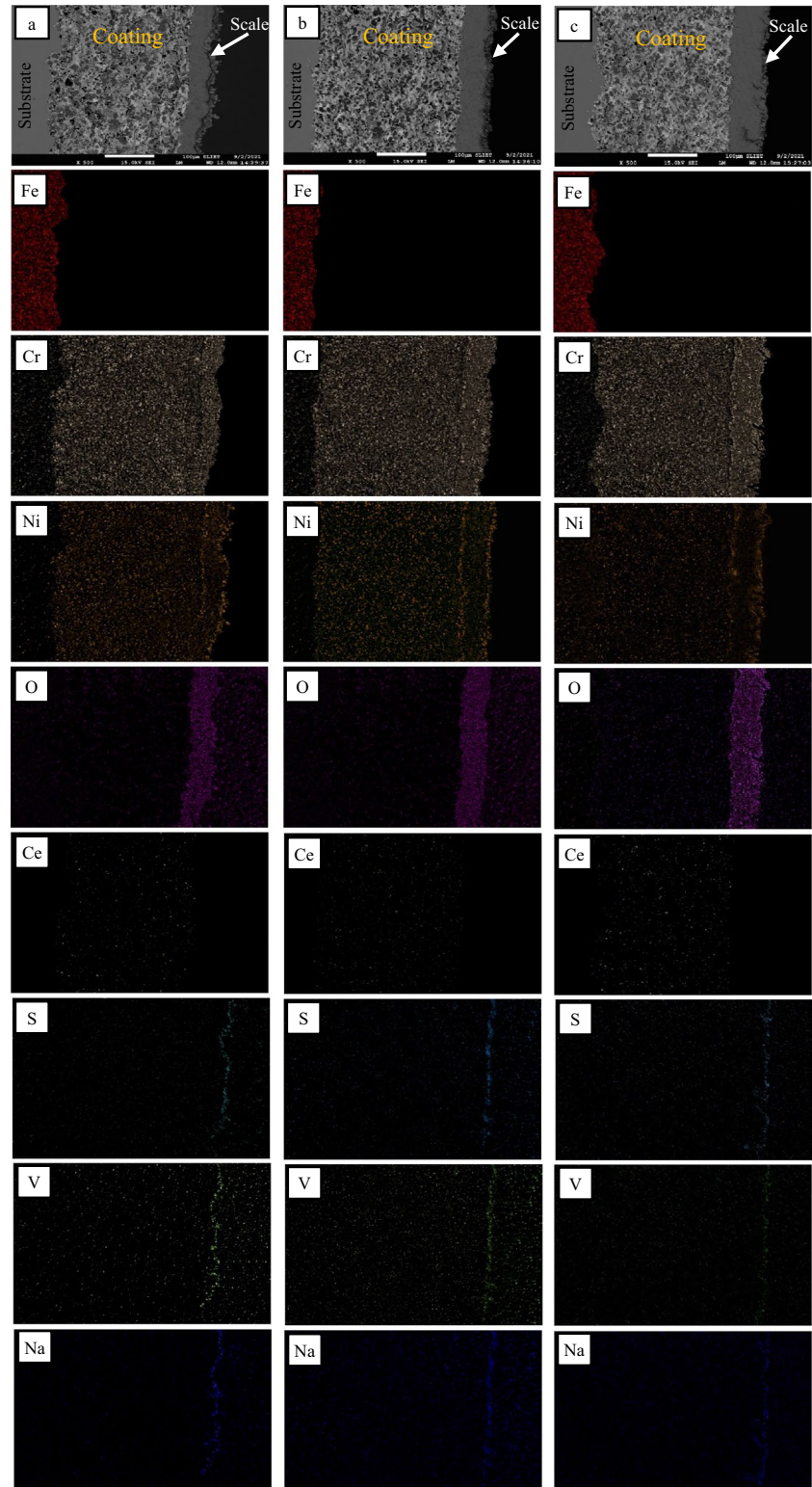


The melting point (610 °C) of the NaVO_3 eutectic mixture is much lower than the current investigation (750 °C). So, it easily combines with the Cr_2O_3 oxide scale according to the following steps [72, 73].



Sodium vanadyl vanadate compound consumes Cr from the oxide scale after forming Na_2CrO_4 , which is a volatile phase that can be evaporated as gas [74]. Moreover, the surface SEM Fig. 9c depicts cracks in the coating, which might be due to the stress generated after heating and cooling cycles. These stresses (compressive/tensile) directly

Fig. 14 Mapping analysis of **a** $\text{Cr}_3\text{C}_2\text{-NiCr} + \text{CeO}_2$ (0.4 wt.%) coated, **b** $\text{Cr}_3\text{C}_2\text{-NiCr} + \text{CeO}_2$ (0.8 wt.%), and **c** $\text{Cr}_3\text{C}_2\text{-NiCr} + \text{CeO}_2$ (1.2 wt.%) coated TP347H steel after subjecting to $\text{Na}_2\text{SO}_4\text{-V}_2\text{O}_5$ salt environment at 750 °C for 50 cycles

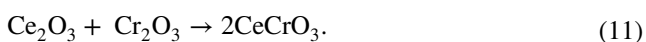


affect the plasticity of the oxide scale, which is released after deformation/cracking through the oxide scale [75].

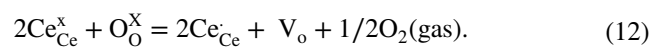
RE element in the $\text{Cr}_3\text{C}_2\text{-NiCr}$ coating successfully reduces the concentration of Cr towards the top of the coatings, which is parallelly confirmed from surface EDS,

cross-sectional, and X-rays mapping results. EDS points 1 and 2 (Fig. 10b) represent the lower weight percentage of Cr (52.56%, 56.23%) and Ni (10.34%, 8.26%) along with Ce (0.37%, 0.52%), suggesting the formation of oxides of the above elements in the presence of oxygen under

salt environment. Moreover, the x-sectional point analysis (Fig. 12c) for HS1-coated steel also illustrates that the RE element (CeO_2) reduces Cr migration towards the top surface of the coating. Due to the lower diffusion of chromium for HS1-coated steel produces thin (Approx. 40 μm) and compact oxide scale of Cr_2O_3 along with spinels of NiCr_2O_4 CeCrO_3 phases. The above oxides and spinels of Cr and Ni formed after reactions, as illustrated in Eqs. 3 and 4. Similarly, oxides and spinels of Ce and Cr developed after the decomposition of CeO_2 and the reaction of Cr_2O_3 and CeO_2 according to the following relations [76].



Various authors [65] [77, 78] reported that Cr_2O_3 , NiCr_2O_4 , and CeCrO_3 phases are thermodynamically stable in various aggressive environments. Moreover, the molten salt phases, Na_2SO_4 and NaVO_3 , could not penetrate through the oxide scale, which shows the protective nature of the coating. The above improvement in the oxide scale might be due to the combined effect of ‘heterogeneous nucleation’ and ‘segregation’ mechanisms done in the presence of ceria [79]. In the heterogeneous nucleation mechanism, CeO_2 acts as a nucleation site for the newly developed grains, resulting in a small grain size, which increases the microhardness and reduces the microporosity of the coated steel [80]. Moreover, the protective oxide scale is produced rapidly due to decreased critical nucleation energy caused by decreased surface tension and interfacial energy [81]. Another improvement of the oxide scale was done by CeCrO_3 after segregating to grain boundaries. Zinkevich [82] and Ashraf Lone [83] reported that the ionic radius of cerium (Ce^{3+} and Ce^{4+}) is larger than Cr cations and Ni cations, and from oxygen anions, which acts as a barrier (hindrance) towards cation diffusion after segregating at grain boundaries resulting in a change in the oxide growth mechanism by cation diffusion to anion diffusion. Hence, the oxide scale is produced with limited thickness, as estimated from the x-sectional SEM analysis for the HS1-coated sample (Fig. 12c). Moreover, due to the change in the mechanism of diffusion, the density (compactness) of HS1-coated steel is greatly enhanced, which might be the reason for the highest corrosion resistance observed under the molten salt environment. RE element (Ce) has a unique property of releasing/storing oxygen at high temperatures, resulting in the decomposition of ceria from (+ 4 oxidation state) to Ce_2O_3 (+ 3 oxidation state) [84, 85]. When cerium changes from Ce^{4+} to Ce^{3+} state, resulting in oxygen vacancies formation, which is represented by the Kroger–Vink notation [86, 87]:



These oxygen vacancies play a vital role in mass diffusion. The defect of oxygen vacancies concentration depends on the dopant content and the degree of reaction [88, 89]. The initial oxidation rate is determined by the migration of oxygen inward through the oxygen vacancies existing in the ceria-modified coating at high temperatures. The availability of oxygen increases with the concentration (wt-%) of dopant in the coating at high temperatures [90]. The above improvement decreases the critical concentration of chromium to form the Cr_2O_3 layer [46]. Once the protective layer forms on the surface of the coating, it achieves steady-state oxidation [91] and impedes the diffusion of oxygen and molten salt corroding species (Na, V, and S), as confirmed by the x-rays mapping analysis (Fig. 14a). Moreover, cerium oxide also slows down the fluxing action of NaVO_3 [92].

In the case of HS3-coated steel, the weight percentage of CeO_2 is increased from 0.4 wt.% to 0.8 wt.% results in microhardness increases from 813 to 840.9 Hv. EDS analysis points 1 and 2 (Fig. 10d) represent the weight percentage of Cr (56.49%, 59.29%) and Ni (12.63%, 10.40%) along with Ce (0.92%, 0.76%), suggesting the formation of oxides of above elements in the presence of oxygen under salt environment. Moreover, the x-sectional point analysis (Fig. 12d) for HS3-coated steel also illustrates that the presence of CeO_2 reduces the amount of Cr needed for the oxide scale. In this case, HS3-coated steel developed approx. 55 μm thick oxide scale of Cr_2O_3 along with spinels of NiCr_2O_4 , and Ce_2O_3 , CeCrO_3 phases as validated by XRD diffractograms (Fig. 8d) and x-rays mapping (Fig. 14b). According to previous equations, the identified phases of Cr and Ni, and Ce may have developed after the chemical reactions (Eqs. 3, 4, 9–11). Molten salt phases such as Na_2SO_4 , NaVO_3 , and V_2O_5 could not diffuse into the oxide scale, which can be authenticated by the x-rays mapping analysis depicted in Fig. 14b. There was no cracking and spallation during the hot corrosion study, as seen from the pictorial view of hot corroded HS3-coated steel (Fig. 6d). Moreover, the ratio of CeO_2 (0.8 wt%) is higher than the HS1-coated steel, resulting in higher oxygen vacancies generated by the RE element, as discussed in the previous section. Due to the above effect, more Cr migrates (cation diffusion) towards the oxygen vacancies to form the Cr_2O_3 scale along with Ce.

Figure 8e represents the XRD profile for the HS5 coated sample after the hot corrosion study, which illustrated that the oxide scale primarily consisted of Cr_2O_3 , NiCr_2O_4 , Ce_2O_3 , CeCrO_3 , Na_2SO_4 , and NaVO_3 phases. The above-identified phases of Cr and Ni, along with Ce, were reported to be protective by various authors [93, 94] during oxidation and hot corrosion studies in different aggressive environments. EDS points 1 and 2 (Fig. 11b) after hot corrosion cycles show higher wt.% of Cr as compared to HS1

(Fig. 10b) and HS3 (Fig. 10d) coated samples, which is confirmed by x-sectional point analysis (Fig. 12e). In this case, HS5-coated steel developed approximately 70- μm -thick oxide scale on the coating surface, which could not provide protection as offered by HS1- and HS3-coated samples. The cross-sectional SEM depicts the oxide scale that experienced a hot corrosion attack, validated by x-rays mapping analysis, as shown in Fig. 14c. The excessive wt. ratio of CeO_2 may have produced coating defects such as microporosity and inclusions in the coating, which reduces its adhesion and plasticity of the oxide scale [95]. Various authors have [96–100] reported that a high ratio (wt.%) of rare earth elements promotes oxygen vacancies concentration and nucleation sites for the oxide scale but also promotes porosity/cavities inside the oxide scale, which might be due to the difference between oxygen vacancies and chromia nucleation sites. The gap that arises between vacancies and nucleation sites may reduce oxide scale adhesion, as noticed in the HS5-coated steel. A model describing the formation of corrosion products was established on the basis of the corrosion products, and the corrosion mechanism is described in Fig. 15. The initial and final stages of hot corrosion for the conventional and ceria-modified $\text{Cr}_3\text{C}_2\text{-NiCr} + 0.4 \text{ wt.}\%$ CeO_2 -coated TP347H steel after subjected to $\text{Na}_2\text{SO}_4\text{-V}_2\text{O}_5$

salt at 750 °C for 50 cycles are shown in Fig. 15a–d, respectively. The hot corrosion resistance of the samples under study after subjected to $\text{Na}_2\text{SO}_4\text{-60}\%$ V_2O_5 salt environment at 750 °C is as follows $\text{HS1} > \text{HS3} > \text{HS5} > \text{HS} > \text{TP347H}$.

- HVOF gun successfully deposited cerium blended (0.4 wt.%, 0.8 wt.%, and 1.2 wt.%) and conventional carbide coatings with homogeneous microstructure. Moreover, refinement is observed by the addition of cerium oxide in terms of quality improvement of the $\text{Cr}_3\text{C}_2\text{-NiCr}$ coating, leading to higher microhardness, low surface roughness, and reduction in microporosity compared to the coating without rare earth elements.
- Bare steel TP347H possessed lower weight gain under a molten salt environment. However, cracks observed in the oxide scale were evidenced during the cyclic study. Cr (17.53 wt.%) and Ni (11.42 wt.%) in austenite steel might have protected its base steel after developing spinels of NiFe_2O_4 and NiCr_2O_4 . Nevertheless, the TP347H steel failed due to the development of unprotective oxides of Fe_2O_3 .
- $\text{Cr}_3\text{C}_2\text{-NiCr}$ -coated TP347H steel provided hot corrosion resistance with minor cracks in the thick oxide scale of Cr_2O_3 and NiCr_2O_4 spinels. Cracks in the coating might

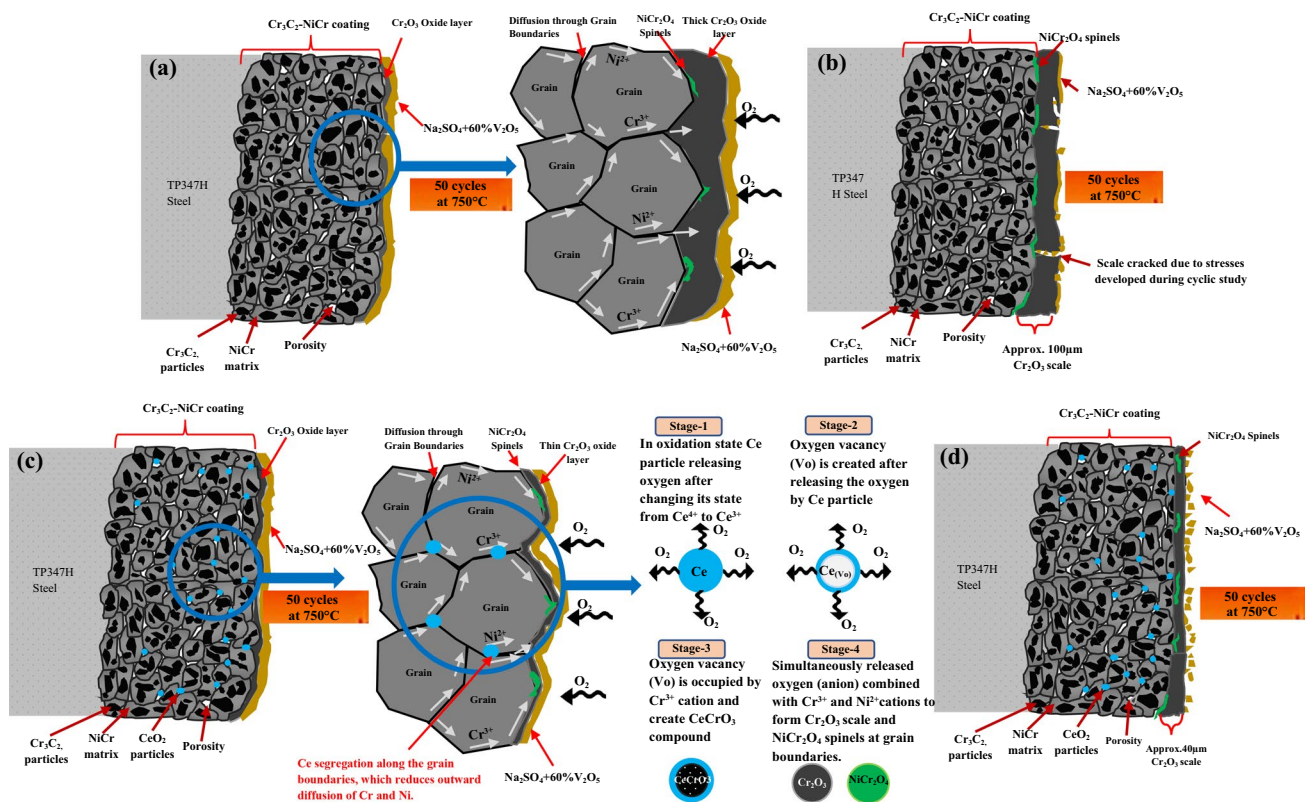


Fig. 15 A proposed mechanism for internal diffusion in undoped $\text{Cr}_3\text{C}_2\text{-NiCr}$ coating **a** initial stage, and **b** final stage and internal diffusion in ceria-doped (0.4 wt%) $\text{Cr}_3\text{C}_2\text{-NiCr}$ coating **c** initial stage, and **d** final stage under the molten salt environment at 750 °C for 50 cycles

be due to thermal stresses developed after the repetition of heating and cooling at 750 °C, which reduces the plasticity of the oxide scale. Moreover, the acidic nature of the NaVO₃ salt compound reduces the oxide scale protection after the dilution of the Cr₂O₃ layer.

- Cr₃C₂-NiCr coating modified with different contents (0.4 wt-%, 0.8 wt-%, and 1.2 wt-%) of CeO₂ provided better protection to the bare TP347H steel than Cr₃C₂-NiCr coating. Moreover, ceria addition in the Cr₃C₂-NiCr coating reduces the amount of Cr required to produce the Cr₂O₃ layer.
- From the ceria-modified Cr₃C₂-NiCr coatings, the HS1-coated (Cr₃C₂-NiCr + 0.4 wt.% CeO₂) steel exhibited better hot corrosion resistance, followed by HS3, and HS5, doped in with 0.8 wt-% and 1.2 wt-% of CeO₂, respectively.
- Modified coatings (HS1, HS3, and HS5) provided better hot corrosion resistance with a thin oxide scale (Approx. 40 μm, 55 μm, and 70 μm) composed of Cr₂O₃, Cr₂₃C₆, Cr₇C₃, NiCr₂O₄, Ce₂O₃, and CeCrO₃ phases. Oxides and spinels of Ce prevent metal ions (cation diffusion) from migrating outward, resulting in a thin oxide layer on the coating's surface. However, the higher ratio (1.2 wt.%) of CeO₂ in the Cr₃C₂-NiCr coating could not adequately protect from hot corrosion, which might be due to the higher porosity, as reported in Table 4. The conventional coating (HS) and the ceria-modified (HS5, 1.2 wt.%) coating provided equal protection.
- NaVO₃ and Na₂SO₄, along with V₂O₅ phases, were mainly responsible for the depletion of protective oxides and spinels.

Author Contributions All the authors have equally participated and worked as a team to complete this research work. The major contribution of the authors is listed as: HS: Problem formulation, related literature review, fabrication of the experimental set-up, and procurement of material, conducting of experimentation, testing, analysis of the results, and writing—original draft are the major contribution of the HS. SSC, BSS: Discussion on the idea, help in the procurement and arranging of the facilities, conducting of experimentation, analysis of the results, writing—review and editing, and whole process monitoring are the major contributions of the SSC and BSS.

Funding No grants received for this research.

Data Availability Statement The data used to support the findings of this study are included within the article.

Declarations

Conflict of interest Authors declare that they have no conflicts of interest of any sort.

References

1. Tang P, He D, Li W et al (2020) Achieving superior hot corrosion resistance by PVD/HVOF duplex design. *Corros Sci* 175:108845. <https://doi.org/10.1016/j.corsci.2020.108845>
2. Kumar R (2021) Sodium sulphate and V₂O₅-induced hot corrosion kinetics and oxides characteristics of the weldments in SA213 T11 steels. *Mater Lett* 301:130359. <https://doi.org/10.1016/j.matlet.2021.130359>
3. Xu L, Ma S, Fu H (2020) Editorial: advanced corrosion wear resistant alloys and their characterization for high-temperature applications. *Front Mater* 7:280–284. <https://doi.org/10.3389/fmats.2020.00059>
4. Jithesh K, Arivarasu M (2019) An investigation on hot corrosion and oxidation behavior of cobalt-based superalloy L605 in the simulated aero-engine environment at various temperatures. *Mater Res Express*. <https://doi.org/10.1088/2053-1591/ab54dd>
5. Hu S, Finklea H, Liu X (2021) A review on molten sulfate salts induced hot corrosion. *J Mater Sci Technol* 90:243–254. <https://doi.org/10.1016/j.jmst.2021.03.013>
6. Meier GH (2022) Invited review paper in commemoration of over 50 years of oxidation of metals: current aspects of deposit-induced corrosion. *Oxid Met* 98:1–41. <https://doi.org/10.1007/s11085-020-10015-6>
7. De la Roche J, Alvarado-Orozco JM, Toro A (2021) Hot corrosion mechanism of yttria-stabilized zirconia powder in the presence of molten Na₂SO₄ + V₂O₅ salts. *Rare Met* 40:1307–1316. <https://doi.org/10.1007/s12598-020-01388-3>
8. Xiang J, Xie F, Wu X, Wang S (2021) Comparative investigation of oxidation behavior and hot corrosion behavior in NaCl–Na₂SO₄ mixture for a Ti₂AlNb based alloy at 1023 K. *Intermetallics* 132:107151. <https://doi.org/10.1016/j.intermet.2021.107151>
9. Meimaroglou D, Florez D, Hu G-H (2022) A kinetic modeling framework for the peroxide-initiated radical polymerization of styrene in the presence of rubber particles from recycled tires. *Chem Eng Sci* 248:117137. <https://doi.org/10.1016/j.ces.2021.117137>
10. Rahimi A, Shamanian M, Atapour M (2021) Effect of pulse current frequency on microstructure and hot corrosion behavior of Tungsten inert gas-welded joints of N155 superalloy. *J Mater Eng Perform* 30:10. <https://doi.org/10.1007/S11665-021-05878-Y> (30:7494–7509)
11. Pan P, Zhou W, Zhao Y et al (2022) Hot corrosion behavior of an arc sprayed Fe-based amorphous coating in a simulated biomass firing environment. *Corros Sci* 194:109938. <https://doi.org/10.1016/J.CORSCI.2021.109938>
12. Pavlík V, Boča M, Kityk A (2022) Accelerated corrosion testing in molten fluoride salts: effect of additives and the crucible material. *Corros Sci* 195:110011. <https://doi.org/10.1016/J.CORSCI.2021.110011>
13. de la Roche J, Alvarado-Orozco JM, Gómez PA et al (2022) Hot corrosion behavior of dense CYSZ/YSZ bilayer coatings deposited by atmospheric plasma spray in Na₂SO₄ + V₂O₅ molten salts. *Surf Coat Technol* 432:128066. <https://doi.org/10.1016/J.SURFCOAT.2021.128066>
14. Sundaresan C, Rajasekaran B, Varalakshmi S et al (2021) Comparative hot corrosion performance of APS and Detonation sprayed CoCrAlY, NiCoCrAlY and NiCr coatings on T91 boiler steel. *Corros Sci* 189:109556. <https://doi.org/10.1016/J.CORSCI.2021.109556>
15. Mannava V, SambasivaRao A, Kamaraj M, Kottada RS (2019) Influence of two different salt mixture combinations of Na₂SO₄-NaCl-NaVO₃ on hot corrosion behavior of Ni-base

- superalloy Nimonic 263 at 800 °C. *J Mater Eng Perform* 28:1077–1093. <https://doi.org/10.1007/s11665-019-3866-4>
16. Song P, Liu M, Jiang X et al (2021) Influence of alloying elements on hot corrosion resistance of nickel-based single crystal superalloys coated with Na₂SO₄ salt at 900 °C. *Mater Des* 197:109197. <https://doi.org/10.1016/J.MATDES.2020.109197>
 17. Iaiani M, Tugnoli A, Macini P, Cozzani V (2021) Outage and asset damage triggered by malicious manipulation of the control system in process plants. *Reliab Eng Syst Saf* 213:107685. <https://doi.org/10.1016/J.RESS.2021.107685>
 18. Palacios A, Navarro ME, Jiang Z et al (2020) High-temperature corrosion behaviour of metal alloys in commercial molten salts. *Sol Energy* 201:437–452. <https://doi.org/10.1016/J.SOLENER.2020.03.010>
 19. Lutz BS, Yanar NM, Holcomb GR, Meier GH (2016) Fire-side corrosion of alumina-forming austenitic (AFA) Stainless Steels. *Oxid Metals* 87:575–602. <https://doi.org/10.1007/S11085-016-9687-Z>
 20. Kamal S, Sharma KV, Srinivasa Rao P, Mamat O (2017) Thermal spray coatings for hot corrosion resistance. *Top Min Metall Mater Eng*. https://doi.org/10.1007/978-3-319-29761-3_10
 21. Derelizade K, Rincon A, Venturi F et al (2022) High temperature (900 °C) sliding wear of CrNiAlCY coatings deposited by high velocity oxy fuel thermal spray. *Surf Coat Technol*. <https://doi.org/10.1016/J.SURFCOAT.2021.128063>
 22. Yao HL, Yang C, Yi DL et al (2020) Microstructure and mechanical property of high velocity oxy-fuel sprayed WC-Cr₃C₂-Ni coatings. *Surf Coat Technol* 397:126010. <https://doi.org/10.1016/j.surfcoat.2020.126010>
 23. Medved' D, Ivor M, Chmielewski T et al (2020) Microstructure characteristics, tribology and nano-hardness of plasma sprayed nickel coating. *Defect Diffus Forum* 405 DDF:430–434. <https://doi.org/10.4028/www.scientific.net/DDF.405.430>
 24. Jha S, Mishra RS (2021) Mechanical and Tribological behaviour of velocity oxygen fuel thermal spray coating: a review. *J Phys Conf Ser*. <https://doi.org/10.1088/1742-6596/1950/1/012014>
 25. Aghili SE, Shamanian M, Amini Najafabadi R et al (2020) Microstructure and oxidation behavior of NiCr-chromium carbides coating prepared by powder-fed laser cladding on titanium aluminide substrate. *Ceram Int* 46:1668–1679. <https://doi.org/10.1016/j.ceramint.2019.09.139>
 26. Sidhu TS, Prakash S, Agrawal RD (2006) Characterizations and hot corrosion resistance of Cr₃C₂-NiCr coating on Ni-base superalloys in an aggressive environment. *Proc Int Therm Spray Conf* 15:811–816. <https://doi.org/10.1361/105996306X147162>
 27. Sidhu TS, Prakash S, Agrawal RD (2006) Hot corrosion resistance of high-velocity oxyfuel sprayed coatings on a nickel-base superalloy in molten salt environment. *J Therm Spray Technol* 15:387–399. <https://doi.org/10.1361/105996306X124392>
 28. Sidhu TS, Prakash S, Agrawal RD (2006) Hot corrosion studies of HVOF sprayed Cr₃C₂-NiCr and Ni-20Cr coatings on nickel-based superalloy at 900 °C. *Surf Coat Technol* 201:792–800. <https://doi.org/10.1016/j.surfcoat.2005.12.030>
 29. Sidhu TS, Prakash S, Agrawal RD (2007) Study of molten salt corrosion of high velocity oxy-fuel sprayed cermet and nickel-based coatings at 900 °C. *Metall Mater Trans A* 38:77–85. <https://doi.org/10.1007/s11661-006-9002-8>
 30. Bhatia R, Singh H, Sidhu BS (2014) Hot corrosion studies of HVOF-sprayed coating on T-91 boiler tube steel at different operating temperatures. *J Mater Eng Perform* 23:493–505. <https://doi.org/10.1007/s11665-013-0771-0>
 31. Baiamonte L, Bartuli C, Marra F et al (2019) Hot Corrosion resistance of laser-sealed thermal-sprayed cermet coatings. *Coatings* 9:347. <https://doi.org/10.3390/coatings9060347>
 32. Shi M, Xue Z, Liang H et al (2020) High velocity oxygen fuel sprayed Cr₃C₂-NiCr coatings against Na₂SO₄ hot corrosion at different temperatures. *Ceram Int* 46:23629–23635. <https://doi.org/10.1016/j.ceramint.2020.06.135>
 33. Singh K, Goyal K, Goyal R (2019) Hot corrosion behaviour of different Cr₃C₂-NiCr coatings on boiler tube steel at elevated temperature. *World J Eng* 16:452–459. <https://doi.org/10.1108/WJE-02-2019-0049>
 34. Madhu G, Mrityunjaya Swamy KM, Kumar DA et al (2021) Evaluation of hot corrosion behavior of HVOF thermally sprayed Cr₃C₂-35NiCr coating on SS 304 boiler tube steel. In: *AIP Conference Proceedings*, p 030014. <https://doi.org/10.1063/5.0038279>
 35. Alnaser IA, Yunus M, Alfattani R, Alamro T (2021) High-temperature corrosion of APS- and HVOF-coated nickel-based super alloy under air oxidation and melted salt domains. *Materials* 14:5119. <https://doi.org/10.3390/ma14185119>
 36. Singh A, Goyal K, Goyal R, Krishan B (2021) Hot corrosion behaviour of different ceramics coatings on boiler tube steel at 800 °C temperature. *Journal of Bio- and Tribo-Corrosion* 7:21. <https://doi.org/10.1007/s40735-020-00461-9>
 37. Schütze M (2010) Stress effects in high temperature oxidation. In: *Shreir's Corrosion*. Elsevier, pp 153–179. <https://doi.org/10.1016/B978-044452787-5.00011-1>
 38. Vishnoi M, Murtaza Q, Kumar P (2020) Effect of rare earth elements on coatings developed by thermal spraying processes (TSP)—a brief review. *Mater Today Proc*. <https://doi.org/10.1016/j.matpr.2020.10.439>
 39. Du J, Li F, Li Y et al (2021) The influence of nano-CeO₂ on tribological properties and microstructure evolution of Cr₃C₂-NiCrCoMo composite coatings at high temperature. *Surf Coat Technol* 428:127913. <https://doi.org/10.1016/J.SURFCOAT.2021.127913>
 40. Cai G, Li C (2015) Effects of Ce on inclusions, microstructure, mechanical properties, and corrosion behavior of AISI 202 stainless steel. *J Mater Eng Perform* 24:3989–4009. <https://doi.org/10.1007/s11665-015-1651-6>
 41. Chen SF, Liu SY, Wang Y et al (2014) Microstructure and properties of HVOF-sprayed NiCrAlY coatings modified by rare earth. *J Therm Spray Technol* 23:809–817. <https://doi.org/10.1007/s11666-014-0097-y>
 42. Wang S, Zheng Z, Zheng K et al (2020) High temperature oxidation behavior of heat resistant steel with rare earth element Ce High temperature oxidation behavior of heat resistant steel with rare earth element Ce. *Mater Res Express* 7:16571. <https://doi.org/10.1088/2053-1591/ab692d>
 43. Levin V, Sridharan M, Maiyalagan T et al (2021) Enhanced electrocatalytic activity of cobalt-doped ceria embedded on nitrogen, sulfur-doped reduced graphene oxide as an electrocatalyst for oxygen reduction reaction. *Catalysts* 12:6. <https://doi.org/10.3390/CATAL12010006>
 44. Sridharan M, Maiyalagan T, Panomsuwan G, Techapiesancha-oenkij R (2021) Enhanced electrocatalytic activity of cobalt-doped ceria embedded on nitrogen, sulfur-doped reduced graphene oxide as an electrocatalyst for oxygen reduction reaction. *Catalysts* 12:6. <https://doi.org/10.3390/catal12010006>
 45. Yu L, Zhang Y, Fu T et al (2021) Rare earth elements enhanced the oxidation resistance of Mo-Si-based alloys for high temperature application: a review. *Coatings*. <https://doi.org/10.3390/coatings11091144>
 46. Li X, Shu J, Chen L, Bi H (2014) Effect of cerium on high-temperature oxidation resistance of 00Cr17NbTi ferritic stainless steel. *Acta Metall Sin (English Letters)* 27:501–507. <https://doi.org/10.1007/s40195-014-0079-6>
 47. Buzaianu A, Motoiu P, Csaki I et al (2018) Structural properties Ni20Cr10Al2Y coatings for geothermal conditions. *Proceedings* 2:1434. <https://doi.org/10.3390/proceedings2231434>

48. Kevin PS, Tiwari A, Seman S et al (2020) Erosion-corrosion protection due to Cr₃C₂-NiCr cermet coating on stainless steel. *Coatings* 10:1–17. <https://doi.org/10.3390/coatings10111042>
49. Treewiriyakitja P, Thongyoung P, Pokwitidkul S, Tungtrong-pairoj J (2021) The degradation of austenitic stainless steel at high temperature in simulated carbon monoxide containing atmosphere of biomass-to-liquid plants. *IOP Conf Ser Mater Sci Eng* 1163:012022. <https://doi.org/10.1088/1757-899X/1163/1/012022>
50. Yi W, Zheng C, Fan P et al (2000) Effect of rare earth on oxidation resistance of iron base fluxing alloy spray-welding coating. *J Alloy Compd* 311:65–68. [https://doi.org/10.1016/S0925-8388\(00\)00863-X](https://doi.org/10.1016/S0925-8388(00)00863-X)
51. Cai Y, Luo Z, Chen Y (2018) Effect of CeO₂ on TiC morphology in Ni-based composite coating. *High Temp Mater Processes (London)* 37:209–217. <https://doi.org/10.1515/htmp-2016-0198>
52. Wang W, Chen Z, Feng S (2019) Effect of CeO₂ on impact toughness and corrosion resistance of WC reinforced Al-based coating by laser cladding. *Materials* 12:1–15. <https://doi.org/10.3390/ma12182901>
53. Hao M, Sun B, Wang H (2020) High-temperature oxidation behavior of Fe–1Cr–0.2Si Steel. *Materials* 13:509. <https://doi.org/10.3390/ma13030509>
54. Nyadongo ST, Pityana SL, Olakanmi EO (2021) Isothermal oxidation performance of laser cladding assisted with preheat (Lcap) triballoy t-800 composite coatings deposited on en8. *Coatings*. <https://doi.org/10.3390/coatings11070843>
55. Mobin M, Hasan SK (2012) Chemical interaction of ferric oxide with sodium sulfate at high temperature relevant to hot corrosion. *J Mater Environ Sci* 3:109–114
56. Chen K, Lin J, Li W et al (2021) Improved oxidation and hot corrosion resistance of 1Cr11Ni2W2MoV stainless steel at 650 °C by a novel glass-ceramic coating. *Crystals* 11:1213. <https://doi.org/10.3390/cryst11101213>
57. Dudziak T, Jura K (2016) High temperature corrosion of low alloyed steel in air and salt mist atmospheres. *Prace Instytutu Odlewnictwa* 56:77–85. <https://doi.org/10.7356/iod.2016.07>
58. Wang H, Du H, Wei Y et al (2021) Precipitation and properties at elevated temperature in austenitic heat-resistant steels—a review. *Steel Res Int* 92:1–12. <https://doi.org/10.1002/srin.202000378>
59. Silva-Leon PD, Sotelo-Mazon O, Salinas-Solano G et al (2019) Hot corrosion behavior of Ni20Cr alloy in NaVO₃ molten salt. *J Mater Eng Perform* 28:5047–5062. <https://doi.org/10.1007/s11665-019-04235-4>
60. Liu Q, Barker R, Wang C et al (2022) The corrosion behaviour of stainless steels and Ni-based alloys in nitrate salts under thermal cycling conditions in concentrated solar power plants. *Sol Energy* 232:169–185. <https://doi.org/10.1016/J.SOLENER.2021.12.072>
61. Liu H, Huang Y, Wang X, Lu R (2020) Effect of CeO₂ on high-temperature oxidation performance of electron beam cladding NiCoCrAlY coating on Ni-based alloy. *Adv Mater Sci Eng*. <https://doi.org/10.1155/2020/8731315>
62. Zhai W, Gao Y, Sun L et al (2018) Improvement of high temperature oxidation behavior of Cr₃C₂-20 wt % Ni cermets by adding 1 wt % Mo. *J Alloy Compd* 731:271–278. <https://doi.org/10.1016/j.jallcom.2017.10.012>
63. Velikanova TY, Bondar AA, Grytsiv AV (1999) Chromium-nickel-carbon (Cr-Ni-C) phase diagram. *J Phase Equilib* 20:125–147. <https://doi.org/10.1007/s11669-999-0011-3>
64. Wu S, Guo B, Li T, Gui D (2015) Oxidation of chromium carbide coated Q235 steel in wet and dry air at 750°C. *Constr Build Mater* 81:11–14. <https://doi.org/10.1016/j.conbuildmat.2015.01.072>
65. Hong Y, Beyramali Kivy M, Asle Zaeem M (2019) Competition between formation of Al₂O₃ and Cr₂O₃ in oxidation of Al_{0.3}CoCrCuFeNi high entropy alloy: a first-principles study. *Scripta Mater* 168:139–143. <https://doi.org/10.1016/j.scriptamat.2019.04.041>
66. Nyadongo ST, Pityana SL, Olakanmi EO (2021) Isothermal oxidation performance of laser cladding assisted with preheat (LCAP) Triballoy T-800 composite coatings deposited on EN8. *Coatings* 11:843. <https://doi.org/10.3390/coatings11070843>
67. Wei L, Han L, Chen L, Zhao Y (2018) Oxidation behavior of cerium and tungsten-containing ferritic stainless steels at 1200 °C in air. *Proc Manuf* 15:1588–1595. <https://doi.org/10.1016/j.promfg.2018.07.308>
68. Chatha SS, Sidhu HS, Sidhu BS (2012) High temperature hot corrosion behaviour of NiCr and Cr₃C₂-NiCr coatings on T91 boiler steel in an aggressive environment at 750°C. *Surf Coat Technol* 206:3839–3850. <https://doi.org/10.1016/j.surfcoat.2012.01.060>
69. Gheno T, Gleeson B (2015) On the hot corrosion of nickel at 700 °C. *Oxid Met* 84:567–584. <https://doi.org/10.1007/s11085-015-9588-6>
70. Wei B, Chen C, Xu J et al (2022) Comparing the hot corrosion of (100), (210) and (110) Ni-based superalloys exposed to the mixed salt of Na₂SO₄-NaCl at 750 °C: Experimental study and first-principles calculation. *Corros Sci* 195:109996. <https://doi.org/10.1016/J.CORSCI.2021.109996>
71. Amiri Kerahoodi MS, Rahmani K, Yousefi M (2018) The inhibitory effect of magnesium sulfonate as a fuel additive on hot corrosion of generating tubes of power plant boiler. *Oxid Met* 89:565–588. <https://doi.org/10.1007/s11085-017-9802-9>
72. Salehi Doolabi M, Ghasemi B, Sadrnezhaad SK et al (2017) Hot corrosion behavior and near-surface microstructure of a “low-temperature high-activity Cr-aluminide” coating on inconel 738LC exposed to Na₂SO₄, Na₂SO₄ + V₂O₅ and Na₂SO₄ + V₂O₅ + NaCl at 900 °C. *Corros Sci* 128:42–53. <https://doi.org/10.1016/j.corsci.2017.09.004>
73. Rani A, Bala N, Gupta CM (2017) Accelerated hot corrosion studies of D-gun-sprayed Cr₂O₃-50% Al₂O₃ coating on boiler steel and Fe-based superalloy. *Oxid Met* 88:621–648. <https://doi.org/10.1007/s11085-017-9759-8>
74. Wu Q, Xu Y, Zhang J et al (2019) Corrosion behaviour of TiC particle-reinforced 304 stainless steel in simulated marine environment at 650°C. *ISIJ Int* 59:336–344. <https://doi.org/10.2355/isijinternational.ISIJINT-2018-534>
75. Kumar M, Mudgal D, Ahuja L (2020) Evaluation of high temperature oxidation performance of bare and coated T91 steel. *Mater Today Proc* 28:620–624. <https://doi.org/10.1016/j.matpr.2019.12.232>
76. Li H, Cui X, Chen W (2010) Effect of CeO₂ on high temperature carburization behavior of Mn–Cr–O spinel and chromium oxide. *J Electrochem Soc* 157:C321. <https://doi.org/10.1149/1.3478659>
77. Ziemiak SE, Anovitz LM, Castelli RA, Porter WD (2007) Thermodynamics of Cr₂O₃, FeCr₂O₄, ZnCr₂O₄, and CoCr₂O₄. *J Chem Thermodyn* 39:1474–1492. <https://doi.org/10.1016/j.jct.2007.03.001>
78. Kiryukhantsev-Korneev PV, Sytchenko AD, Gorshkov VA et al (2021) Complex study of protective Cr₃C₂-NiAl coatings deposited by vacuum electro-spark alloying, pulsed cathodic arc evaporation, magnetron sputtering, and hybrid technology. *Ceram Int*. <https://doi.org/10.1016/J.CERAMINT.2021.12.311>
79. Shu D, Cui X, Li Z et al (2020) Effect of the rare earth oxide CeO₂ on the microstructure and properties of the nano-WC-reinforced Ni-based composite coating. *Metals* 10:383. <https://doi.org/10.3390/met10030383>
80. You S, Jiang C, Wang L et al (2022) Effect of CeO₂ nanoparticles on the microstructure and properties of the NiCo-CeO₂ composite coatings. *Vacuum* 196:110765. <https://doi.org/10.1016/J.VACUUM.2021.110765>

81. Lone SA, Rahman A (2020) Hot corrosion behaviour of electrodeposited nano-structured cerium oxide coatings on superalloy. *J Inst Eng (India) Ser D* 101:81–92. <https://doi.org/10.1007/s40033-020-00220-7>
82. Zinkevich M, Djurovic D, Aldinger F (2006) Thermodynamic modelling of the cerium-oxygen system. *Solid State Ionics* 177:989–1001. <https://doi.org/10.1016/j.ssi.2006.02.044>
83. Lone SA, Eatoo MA, Rahman A (2019) Degradation behaviour of nanostructured CeO₂ films on superalloy. *Trans Indian Inst Met* 72:793–800. <https://doi.org/10.1007/s12666-018-1532-4>
84. Botu V, Ramprasad R, Mhadeshwar AB (2014) Ceria in an oxygen environment: surface phase equilibria and its descriptors. *Surf Sci* 619:49–58. <https://doi.org/10.1016/j.susc.2013.09.019>
85. Liu S, Wu X, Weng D, Ran R (2015) Ceria-based catalysts for soot oxidation: a review. *J Rare Earths* 33:567–590. [https://doi.org/10.1016/S1002-0721\(14\)60457-9](https://doi.org/10.1016/S1002-0721(14)60457-9)
86. Muhich CL (2017) Re-evaluating CeO₂ expansion upon reduction: noncounterpoised forces, not ionic radius effects, are the cause. *J Phys Chem C* 121:8052–8059. <https://doi.org/10.1021/acs.jpcc.6b12373>
87. Wen Y, Abe H, Mitsuishi K, Hashimoto A (2021) Tracking the emergence of epitaxial metal–oxide interfaces from precursor alloys. *Nanoscale* 13:18987–18995. <https://doi.org/10.1039/D1NR03492H>
88. Esposito V, Ni DW, He Z et al (2013) Enhanced mass diffusion phenomena in highly defective doped ceria. *Acta Mater* 61:6290–6300. <https://doi.org/10.1016/j.actamat.2013.07.012>
89. Kumar M, Yun JH, Bhatt V et al (2018) Role of Ce³⁺ valence state and surface oxygen vacancies on enhanced electrochemical performance of single step solvothermally synthesized CeO₂ nanoparticles. *Electrochim Acta* 284:709–720. <https://doi.org/10.1016/j.electacta.2018.07.184>
90. Rahman A, Jayaganthan R (2016) Study of nanostructured CeO₂ coatings on superalloy. *Surf Eng* 32:771–778. <https://doi.org/10.1080/02670844.2016.1148381>
91. Wang Q, Yao Q, Song J-Z et al (2017) Effect of rare earth element on the oxidation behavior of novel γ/γ' -strengthened Co–9Al–10W alloys. *J Mater Res* 32:2117–2126. <https://doi.org/10.1557/jmr.2017.14>
92. Mukherjee B, Islam A, Pandey KK et al (2019) Impermeable CeO₂ overlay for the protection of plasma sprayed YSZ thermal barrier coating from molten sulfate-vanadate salts. *Surf Coat Technol* 358:235–246. <https://doi.org/10.1016/j.surfcoat.2018.11.048>
93. Seal S, Nardelli R, Kale A et al (1999) Role of surface chemistry on the nature of passive oxide film growth on Fe–Cr (low and high) steels at high temperatures. *J Vac Sci Technol A Vac Surf Films* 17:1109–1115. <https://doi.org/10.1116/1.581782>
94. de Fernandes SMC, Ramanathan LV (2004) Rare earth oxide coatings to decrease high temperature degradation of chromia forming alloys. *Mater Res* 7:135–139. <https://doi.org/10.1590/s1516-14392004000100018>
95. Pang Q, Hu ZL, Sun DL (2016) The influence of Ce content and preparation temperature on the microstructure and oxidation behavior of Ce–modified Cr coating on open–cell NiCrFe alloy foam. *Vacuum* 129:86–98. <https://doi.org/10.1016/j.vacuum.2016.04.018>
96. Naumenko D, Pint BA, Quadackers WJ (2016) Current thoughts on reactive element effects in alumina-forming systems. in memory of John Stringer. *Oxid Met* 86:1–43. <https://doi.org/10.1007/s11085-016-9625-0>
97. Thanneeru R, Patil S, Deshpande S, Seal S (2007) Effect of trivalent rare earth dopants in nanocrystalline ceria coatings for high-temperature oxidation resistance. *Acta Mater* 55:3457–3466. <https://doi.org/10.1016/j.actamat.2007.01.043>
98. Cambon J-B, Esteban J, Ansart F et al (2012) Effect of cerium on structure modifications of a hybrid sol–gel coating, its mechanical properties and anti-corrosion behavior. *Mater Res Bull* 47:3170–3176. <https://doi.org/10.1016/j.materresbull.2012.08.034>
99. Zand RZ, Verbeken K, Adriaens A (2013) Influence of the cerium concentration on the corrosion performance of ce-doped silica hybrid coatings on hot dip galvanized steel substrates. *Int J Electrochem Sci* 8:548–563
100. Rehman K, Sheng N, Sang Z et al (2021) Comparative study of the reactive elements effects on oxidation behavior of a Ni-based superalloy. *Vacuum* 191:110382. <https://doi.org/10.1016/j.vacuum.2021.110382>

Publisher's Note Springer Nature remains neutral with regard to jurisdictional claims in published maps and institutional affiliations.

Springer Nature or its licensor (e.g. a society or other partner) holds exclusive rights to this article under a publishing agreement with the author(s) or other rightsholder(s); author self-archiving of the accepted manuscript version of this article is solely governed by the terms of such publishing agreement and applicable law.